

SOUND SCATTERING AND ATTENUATION
IN AQUEOUS SUSPENSIONS OF SAND:
COMPARISON OF THEORY AND EXPERIMENT

CENTRE FOR NEWFOUNDLAND STUDIES

**TOTAL OF 10 PAGES ONLY
MAY BE XEROXED**

(Without Author's Permission)

JINYU SHENG



**SOUND SCATTERING AND ATTENUATION IN
AQUEOUS SUSPENSIONS OF SAND: COMPARISON
OF THEORY AND EXPERIMENT**

BY



Jinyu Sheng, B.Sc. (Hons.)

A thesis submitted to the School of Graduate
Studies in partial fulfillment of the
requirements for the degree of
Master of Science

Department of Physics
Memorial University of Newfoundland

May 1986

St. John's

Newfoundland

Permission has been granted to the National Library of Canada to microfilm this thesis and to lend or sell copies of the film.

The author (copyright owner) has reserved other publication rights, and neither the thesis nor extensive extracts from it may be printed or otherwise reproduced without his/her written permission.

L'autorisation a été accordée à la Bibliothèque nationale du Canada de microfilmer cette thèse et de prêter ou de vendre des exemplaires du film.

L'auteur (titulaire du droit d'auteur) se réserve les autres droits de publication; ni la thèse ni de longs extraits de celle-ci ne doivent être imprimés ou autrement reproduits sans son autorisation écrite.

ISBN 0-315-31025-1

ABSTRACT

Theoretical estimates of scattered acoustic intensity and attenuation coefficient are compared with all available data for aqueous suspensions of sand, for both bistatic and monostatic systems. This appears to be the first comparison of theoretical and experimental attenuation coefficients in suspensions of mineral grains at wavelengths comparable to or less than the scatterer circumference, and it is shown that as far as the existing data are concerned, this comparison is crucial. Three theoretical models are used, in which the scatterer is assumed to be either elastic, or completely rigid, or both rigid and immovable. The rigid movable model with a Gaussian size distribution provides the best fit to the data. The failure of the elastic model indicates that resonance excitation does not occur, probably because natural sand grains are irregularly shaped and inhomogeneous in composition. The rigid immovable model fits the data the least well, indicating that the inertia of the particles is important. Approximate expressions for the form factor and attenuation coefficient have been constructed, based on the so-called high-pass model introduced by Johnson [1977]. The high-pass model provides a fit to the data which is as good as the rigid movable case. Multiple scattering is discussed briefly, and approximate estimates of the correction for multiple scattering are made. In addition, the geometry of scattering and attenuation in suspensions for bistatic systems is analyzed for the narrow beam case, and approximate analytical expressions for the detected volume and scattered intensity are obtained.

ACKNOWLEDGEMENTS

It is a pleasure to acknowledge my deepest appreciation and gratitude to my supervisor, Dr. Alex Hay, for his guidance, patience and encouragement throughout the course of this work. I would like to express my thanks to Dr. Ian Webster and Dr. Brian Sanderson and other faculty members in the Department for their advice. I also acknowledge Mr. Douglas Mercer and Mr. Eugene Colbourne for very helpful discussions in computer programming techniques for this project. I am grateful for the assistance from the staff of the Computing Service of the University.

I especially thank Dr. A. Schaafsma (Delft Hydraulics Laboratory) for his cooperation in making data available to me.

I am deeply appreciative of the financial assistance from the Memorial University of Newfoundland in the form of a University Fellowship, Teaching Assistantship, and Dr. Hay's grants (Operating Grant A8446, Natural Sciences and Engineering Research Council of Canada and Research Agreement-152, Department of Energy, Mines and Resources), which supported me during my graduate studies.

Specially, I wish to thank my wife for her understanding and spiritual support during my stay in Canada.

TABLE OF CONTENTS

ABSTRACT	i
ACKNOWLEDGEMENTS	ii
TABLE OF CONTENTS	iii
LIST OF FIGURES	v
LIST OF TABLES	viii

	page
CHAPTER 1 INTRODUCTION	1
1.1 Historical background	2
1.1.1 Scattering by a solid sphere	3
1.2.2 Attenuation in suspensions of solid particles	4
1.2 Current situation and statement of the problem	5
1.3 Approach and thesis outline	6
CHAPTER 2 BASIC THEORY	7
2.1 Scattered pressure from a single particle	7
2.2 Scattered pressure from an ensemble of particles	9
2.3 The bistatic case	11
2.4 The detected volume τ and G^2 for bistatic systems	15
2.4.1 Numerical evaluation of τ and G^2	21
2.4.2 Parabolic approximation for τ and G^2	25
2.5 Multiple scattering limit	30

CHAPTER 3	THE FORM FACTOR	38
3.1	Phase shift formalism	38
3.2	Numerical results	41
3.3	Analytic expressions for $ f_{\infty} $	45
3.4	The dependence of $ f_{\infty} $ on scattering angle	48
CHAPTER 4	THE ATTENUATION COEFFICIENT	51
4.1	Numerical results	53
4.2	Analytic expression for α_s	56
CHAPTER 5	COMPARISON WITH DATA	58
5.1	The data	58
5.2	Measured and theoretical attenuation coefficients	63
5.2.1	Estimating α_s from the measurements	63
5.2.2	Comparison assuming uniform particle size	64
5.2.3	Multiple scattering	72
5.2.4	Size distributions	78
5.2.5	Estimating sand size distribution parameters	82
5.2.6	Comparison with data using size distributions	83
5.3	Measured and theoretical scattering coefficients	86
5.4	Discussion	99
CHAPTER 6	CONCLUSIONS	103
REFERENCES		106
APPENDIX A	The derivations for τ and G^2	109
APPENDIX B	The variation of $ f_{\infty} $ and α_s with elastic constants	112

LIST OF FIGURES

Figure 1.	The geometry of scattering of an acoustic wave by a sphere.	8
Figure 2.	The geometry for the bistatic case. T is the transmitter, R is the receiver. The remaining symbols are defined in the text.	12
Figure 3.	Parabolic approximation of the cross-section in XZ-plane. Π' represents a plane parallel to the XZ-plane, and the ellipses shown are in the Π' plane.	28
Figure 4.	The half-period zone for the first order multiple scattered waves.	32
Figure 5.	Calculated values of $ f_{\infty} $ at scattering angle $\theta = 120^\circ$ for four theoretical models. (a) elastic case; (b) rigid movable case; (c) rigid immovable case; (d) high-pass model.	44
Figure 6.	The form factor in the forward direction for quartz in water.	49
Figure 7.	The difference of $ f_{\infty} $ in the narrow beam pattern.	50
Figure 8.	Calculated values of $\alpha\alpha_s/\epsilon$ for four theoretical models. (a) elastic case; (b) rigid movable case; (c) rigid immovable case; (d) high-pass model.	54
Figure 9.	Calculated values of $\rho_s'\alpha_s/k_c M$ for four theoretical models. (a) elastic case; (b) rigid movable case; (c) rigid immovable case; (d) high-pass model.	55
Figure 10.	The mean square scattered signal as a function of sand concentration for various grain radii (from Jansen [1977]).	60

- Figure 11. The mean square scattered signal from the 2-dimensional system. S_1^2 is the output signal from receiver 1 and S_2^2 is the output signal from receiver 2 (from Schaafsma and der Kinderen [1985]). 62
- Figure 12. $\log_{10}[\bar{p}_s^2/M]$ vs M for data given by Jansen [1977]. (a) at low concentrations; (b) over the entire range of concentration in the experiments for $\bar{\sigma} = 50$ and $120 \mu\text{m}$ (see also Fig. 10). 65
- Figure 13. $\log_{10}[\bar{p}_s^2/M]$ vs M for data given by Schaafsma and der Kinderen [1985]. (a) from S_2^2 ; (b) from S_1^2 (see also Fig. 11). 66
- Figure 14a and b. Comparison of measured and computed values of $\bar{\sigma}\alpha_s/\epsilon$ using Jansen's data. The theoretical curves are for: (a) elastic case; (b) rigid movable case. 68
- Figure 14c and d. Comparison of measured and computed values of $\bar{\sigma}\alpha_s/\epsilon$ using Jansen's data. The theoretical curves are for: (c) rigid immovable case; (d) high-pass model. 69
- Figure 15a and b. Comparison of measured and computed values of $\bar{\sigma}\alpha_s/\epsilon$ using Schaafsma and der Kinderen's data. The theoretical curves are for: (a) elastic case; (b) rigid movable case. 70
- Figure 15c and d. Comparison of measured and computed values of $\bar{\sigma}\alpha_s/\epsilon$ using Schaafsma and der Kinderen's data. The theoretical curves are for: (c) rigid immovable case; (d) high-pass model. 71
- Figure 16. Calculated and measured values of $\bar{\sigma}\alpha_s/\epsilon$ for uniform particle size. (a) elastic case; (b) rigid movable case; (c) rigid immovable case; (d) high-pass model. In these and subsequent figures the solid line represents perfect agreement between theory and experiment, not the best fit straight line. 73
- Figure 17. The geometry in Jansen's experiments. The 3 cm diameter perspex cylinder through which the sand grains were allowed to fall is shown in the center of the sketch. 75

- Figure 18. The Gaussian and Rayleigh distributions. Here a_{cutoff} and a_{cutoff} are the lower and upper cutoff size, respectively. n_0 is the amplitude of $n(a)$. The remaining symbols are defined in the text. 81
- Figure 19. Theoretical estimates of H_0^2/M vs x for uniform size. (a) elastic case; (b) rigid movable case; (c) rigid immovable case; (d) high-pass model. 87
- Figure 20. Normalized values of H_0^2 and $\overline{V_0^2}$ for uniform particle size. (a) elastic case; (b) rigid movable case; (c) rigid immovable case; (d) high-pass model. 90
- Figure 21. Theoretical estimates of H_0^2/M vs x for the Gaussian distribution. (a) elastic case; (b) rigid movable case; (c) rigid immovable case; (d) high-pass model. 92
- Figure 22. Theoretical estimates of H_0^2/M vs x for the Rayleigh distribution. (a) elastic case; (b) rigid movable case; (c) rigid immovable case; (d) high-pass model. 93
- Figure 23. Normalized values of H_0^2 and $\overline{V_0^2}$ for the Gaussian distribution. (a) elastic case; (b) rigid movable case; (c) rigid immovable case; (d) high-pass model. 96
- Figure 24. Normalized values of H_0^2 and $\overline{V_0^2}$ for the Rayleigh distribution. (a) elastic case; (b) rigid movable case; (c) rigid immovable case; (d) high-pass model. 97
- Figure 25. Normalized values of $\rho_0 \alpha_0 / k_0 M$ and $\overline{V_0^2}$. (a) elastic case; (b) rigid movable case; (c) rigid immovable case; (d) high-pass model. 102
- Figure 26. The variation of $|f_\infty|$ in four kinds of sand material. (a) granitic gneiss; (b) granite; (c) mineral quartz; (d) sandstone quartzite. 114
- Figure 27. The variation of $a \alpha_0 / \epsilon$ in four kinds of sand material. (a) granitic gneiss; (b) granite; (c) mineral quartz; (d) sandstone quartzite. 115

LIST OF TABLES

Table 1.	The numerical values of G^2 and the comparison with results of the parabolic approximation.	25
Table 2.	Elastic properties of the sediments used in calculations.	43
Table 3.	The parameters of the acoustic systems. Data sources: (a1) Jansen, [1977]; (a2) Jansen, [1979]; (b1) 1-D and (b2) 2-D from Schaafsma and der Kinderen, [1985] and (c) Clarke et al., [1984]. NS represents "not specified".	59
Table 4.	Calculated and measured values of $\bar{\alpha}\alpha_s/\epsilon$ assuming uniform particle size. Data sources: (a) Jansen, [1977] and [1979]; (b1) 1-D and (b2) 2-D from Schaafsma and der Kinderen, [1985]. "Movable" and "Immovable" refer to the rigid movable case and the rigid immovable case, respectively.	67
Table 5.	The size-distribution parameters.	82
Table 6a.	Calculated and measured values of $\bar{\alpha}\alpha_s/\epsilon$ for the Gaussian size distribution. Data sources: (a) Jansen, [1977] and [1979]; (b1) 1-D and (b2) 2-D from Schaafsma and der Kinderen, [1985]. "Movable" and "Immovable" refer to the rigid movable case and the rigid immovable case, respectively.	84
Table 6b.	Calculated and measured values of $\bar{\alpha}\alpha_s/\epsilon$ for the Rayleigh size distribution.	84
Table 7a.	Root mean square difference between computed and measured values of attenuation coefficient $\bar{\alpha}\alpha_s/\epsilon$.	85

Table 7b.	Root mean square difference between computed and measured values of attenuation coefficient $\beta \bar{\alpha}_s / c$ (considering Schaafsma and der Kinderen's, experiments only):	85
Table 8.	Calculated values of H_s^2 assuming uniform particle size and measured values of mean square scattered signal, V_s^2 . Data sources: (a) Jansen, [1977]; (b1) 1-D and (b2) 2-D from Schaafsma and der Kinderen, [1985]; (c1) the major axis and (c2) the minor axis of sand from Clarke et al., [1984]. "Movable" and "Immovable" refer to the rigid movable case and rigid immovable case, respectively.	89
Table 9a.	Calculated values of H_s^2 for the Gaussian size distribution and measured values of mean square scattered signal, V_s^2 . Data sources: (a) Jansen, [1977]; (b1) 1-D and (b2) 2-D from Schaafsma and der Kinderen, [1985]; (c1) the major axis and (c2) the minor axis of sand from Clarke et al., [1984]. "Movable" and "Immovable" refer to the rigid movable case and rigid immovable case, respectively.	94
Table 9b.	Calculated values of H_s^2 for the Rayleigh size distribution and measured values of mean square scattered signal, V_s^2 . Data sources: (a) Jansen, [1977]; (b1) 1-D and (b2) 2-D from Schaafsma and der Kinderen, [1985]; (c1) the major axis and (c2) the minor axis of sand from Clarke et al., [1984]. "Movable" and "Immovable" refer to the rigid movable case and rigid immovable case, respectively.	95
Table 10.	Root mean square differences between normalized values of H_s^2 and normalized values of V_s^2 .	98
Table 11.	Root mean square differences between normalized values of $\rho_s \alpha_s / k M$ and normalized values of V_s^2 .	101
Table 12.	The non-dimensional eigenfrequencies of the first and the second resonances.	113

CHAPTER 1 INTRODUCTION

The purpose of this thesis is to compare the available experimental data on attenuation and scattering of sound by sand grains in water with different theoretical models. The objective is to determine which model is the most suitable, in order to assist in interpreting the relationship between the scattered acoustic signal, and particle concentration and size. It is of particular interest to determine whether resonance effects are likely to be important for natural sand grains.

The problem is part of the more general one associated with the advent in recent years of acoustic remote sensing techniques in sediment transport studies. Direct sampling methods (traps and pumps) to measure suspended sediment near the sea bed do not meet all requirements since they modify the flow field and usually provide data only at single points. Optical methods offer some improvement, but they cannot be used at high concentrations. The greatest advantage of acoustic techniques over optical and other methods is that acoustic signals can travel much farther in water. This provides the opportunity for quantitative remote detection, and therefore minimal disturbance to the flow field.

1.1 Historical background

Using acoustic methods to obtain estimates of suspended sediment concentration in the ocean was suggested by Dietz [1948]. Little was done for many years, but progress has been rapid in the past decade. Two types of system have been used: monostatic, in which the source and receiver are collocated and the backscattered signal is detected; and bistatic systems, in which the transmitter and receiver are spatially separated, and the detected signal is due to scattering out of the path of the transmitted wave.

Proni et al. [1975, 1976a] used an acoustic sounding system operating at 20 kHz to detect suspended particulate matter arising from dredging operations. Proni et al. [1976b] used a modified acoustic echo sounder operating at 20 and 200 kHz to detect and map sewage sludge dumped into the ocean. Orr and Hess [1978] used an acoustic backscatter system operating at 20 and 200 kHz to detect a near-bottom intrusion of slope water carrying high suspended particulate concentrations onto the continental shelf. Young et al. [1982] and Vincent et al. [1982] employed a bottom-mounted acoustic backscatter system operating at 3 MHz to obtain spatially and temporally detailed profiles of wave-generated suspended sediment in the bottom boundary layer on the continental shelf. Hay et al. [1982] used an acoustic sounder operating at 42.5, 107 and 200 kHz to detect a surge-type turbidity current. Hay [1983] employed a 192 kHz acoustic backscatter system to measure suspended sediment in a negatively buoyant, mine-tailing discharge plume in a submarine channel. Jansen [1977] developed a bistatic system operating at 8 MHz to profile suspended particles. Schaafsma and der Kinderen [1985] used an acoustic bistatic scatterometer operating at 4.5 MHz

to measure vertical profiles of suspended sand concentration in an estuary. All of these studies have demonstrated the utility of acoustic remote sensing techniques with respect to sediment transport problems. One of remaining difficulties in the quantitative use of these techniques involves the choice of the most appropriate acoustic model for the suspended particles.

There are two aspects to the interaction between sound and suspended particles: scattering and attenuation. Attenuation involves both scattering and absorption of energy. The historical developments with respect to these problems are discussed below.

1.1.1 Scattering by a solid sphere.

In the theory of sound scattering by a solid sphere, three cases have been treated. These are the elastic, the rigid movable, and rigid immovable cases. By elastic we mean that the scatterer is both movable and deformable. More precisely, the incident wave can induce displacements of the scatterer's center of mass, and shear and compression waves may propagate within the material. A rigid scatterer is not deformable: no sound waves propagate within it. An immovable scatterer is infinitely dense.

The scattering of sound by a sphere was first investigated mathematically by Rayleigh [1945, first published in 1896]. However, because of the complexity of the mathematical solution, he only considered the limiting case where the scatterers are small compared with the wavelength, the long wavelength limit. Morse [1948] obtained a convenient form for the scattered wave for the case in which

the scatterers are rigid, but not necessarily small compared to the wavelength. Faran [1951] expanded the study of Morse to obtain solutions for sound scattering by uniform cylinders and spheres of solid elastic material. Faran appears to have been the first to show, both theoretically and experimentally, that the back-scattered amplitude is a minimum at the resonant frequencies of elastic solid scatterers. Using Faran's approach, Hickling [1962] and Hickling and Wang [1965] calculated the backscattered intensity from solid spheres of different materials in water, including the rigid movable case.

The theory has been verified experimentally by Neubauer et al. [1974] and Dragonette et al. [1974], who measured the acoustic pressure backscattered from aluminum and tungsten-carbide spheres over a wide range of frequencies and obtained good agreement with theory, including resonance effects.

1.1.2 Attenuation in suspensions of solid particles

The theoretical study of sound attenuation in dilute suspensions was first considered theoretically by Sewell [1910]. He considered the long wavelength limit for rigid infinitely dense (immovable) spherical particles. A modified exposition of Sewell's method was given by Lamb [1945], who removed the restriction that the particles be immovable. He obtained an expression for the absorption by finding the average rate at which work is done over a large spherical surface surrounding the particle. Epstein and Carhart [1953] refined the theory to include thermal and viscous losses and all wavelengths, but only for fluid spheres. Allegra and Hawley [1972] extended the work of Epstein and Carhart to include elastic solid spheres.

Allegra and Hawley's theory is quite general, reducing to the earlier results in the appropriate limits.

For small particles, Lamb's theory has been verified experimentally by Urlick [1948], who measured the absorption of sound in sand and kaolin suspensions, and by Stakutis et al. [1955], who measured attenuation of ultrasound in suspensions of fine quartz sand. Allegra and Hawley [1972] also measured attenuation coefficients in suspensions of small polystyrene spheres and found good agreement with their theory.

1.2 Current situation and statement of the problem

Hay and Burling [1982] used the Allegra and Hawley theory to extend Paran's solutions to include effects of thermal conductivity and viscosity at long wavelengths. Hay and Mercer [1985] were able to incorporate the viscosity alone at medium and short wavelengths, and showed explicitly that viscous effects on the scattered wave may be ignored for mineral grains suspended in water.

Jansen [1977] and Schaafsma and der Kinderen [1985] reported laboratory measurements of scattered intensity for suspensions of sand grains as a function of sand grain size, but comparisons with theory were not given. Clarke et al. [1984] reported measurements of the acoustic intensity backscattered from sand grains and compared the results with theory, but found that a fluid sphere model provided semi-quantitative agreement with the data.

The use of a fluid sphere model for scattering by solid particles is not very appealing, however, and a more complete comparison between theory and data is

necessary. In particular, comparisons using all available experimental data and including both scattering cross-sections and attenuation coefficients are required. This is undertaken in this thesis and, as will be seen, the comparisons between theoretical and experimental attenuation coefficients are critically important.

1.3 Approach and thesis outline

In this thesis we follow the approach used by Hay and Mercer [1985] and make theoretical estimates of scattering and attenuation coefficients by approximating the sand grain as a homogeneous, spherical scatterer, and by using the phase shift formalism in the partial wave expansion of the pressure field. The theoretical estimates are made for scatterers which are either elastic, rigid, or rigid and immovable and are then compared with the experimental data to determine which model is most appropriate.

The organization of the thesis is as follows. In Chapter 2 a detailed analysis is made for sound scattering from aqueous suspensions in the bistatic geometry. It also includes a brief discussion of multiple scattering. In Chapter 3 we discuss the theory for the amplitude of the wave scattered by a sphere, and in Chapter 4 the attenuation coefficient. In addition to the different theoretical models, approximate expressions are presented. In Chapter 5 we compare these results with data, including the effects of size distributions. Approximate estimates of multiple scattering effects are also made. The conclusions of the study are presented in Chapter 6.

CHAPTER 2 BASIC THEORY

In this chapter we derive the basic equations for the scattered wave in a bistatic system by beginning with discussion of the scattered wave from a single particle. Then, by considering scattering from an ensemble of particles in the detected volume, the factors of geometry and of size distribution are included. Brief consideration is also given to the concentration range in which the multiple scattering effects may be ignored.

2.1 Scattered pressure from a single particle

Assume that a plane sound wave traveling through a fluid medium is incident on an isotropic elastic sphere. Let the center of the particle coincide with the origin of a spherical polar coordinate system, and the plane wave approach the particle along the positive polar axis (Z -axis), as shown in Fig. 1. Ignoring attenuation for the moment, the instantaneous pressure of the incident wave is given by the real part of

$$p_i = p_0 \exp[i(k_z Z - \omega t)] \quad (2.1)$$

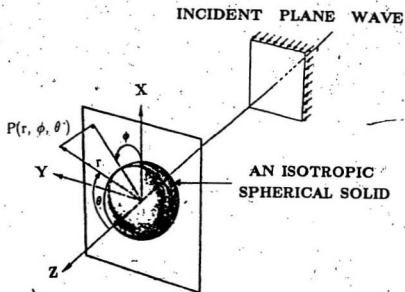


Figure 1. The geometry of scattering of an acoustic wave by a sphere.

where p_0 is the pressure amplitude, ω is the acoustic frequency and k_c the acoustic wavenumber ($= \omega/c$, c being the acoustic phase speed).

The scattered pressure at an arbitrary field point $P(r, \phi, \theta)$ outside the particle is given by

$$p_s = p_0 \left[\frac{a f_{\infty}(\theta, a)}{2r} \right] \exp[i(k_c r - \omega t)] \quad (2.2)$$

where r is the radial coordinate, a is the radius of the particle, θ is the scattering angle (see Fig. 1), and $f_{\infty}(\theta, a)$ is the far field form factor, which is determined by the properties of the scatterer and is discussed in Chapter 3.

2.2 Scattered pressure from an ensemble of particles

In the case of more than one particle, we use the subscript j to refer to different particles, such that, from Eq. (2.2), the scattered pressure at $P(r_j, \phi_j, \theta_j)$ from the j th particle is

$$p_{s,j} = p_0 \left[\frac{a_j f_{\infty}(\theta_j, a_j)}{2r_j} \right] \exp[i(k_c r_j - \omega t)] \quad (2.3)$$

where r_j stands for the distance between the point $P(r_j, \phi_j, \theta_j)$ and the center of j th scatterer.

The total scattered pressure from all scatterers in the ensemble depends on whether a pulsed or continuous wave detection system is used [e.g. Hay, 1983].

Define \hat{p}_r as the *rms* pressure of the return signal. For a continuous wave detection system, because the relative positions of the scatterers within the detected volume change randomly with time, the scattered waves are incoherent, so that

$$\hat{p}_r^2 = \sum_{j=1}^{N\tau} p_{rj} p_{rj}^* \quad (2.4)$$

where N is the number of particles per unit volume, τ is the total detected volume, and p_{rj}^* is the complex conjugate of p_{rj} .

For typical pulsed detection systems, however, the duration of the transmitted pulse is much less than the time required for the relative positions of the scatterers to change by an acoustic wavelength, so the scattered waves from a single pulse are coherent. From pulse to pulse, however, the scattered waves are incoherent. This means that the signal amplitude is Rayleigh-distributed from pulse to pulse, and it has been shown [Hay, 1983] that the pulse-to-pulse rms pressure is given by

$$\hat{p}_r^2 = \frac{\pi}{4} \sum_{j=1}^{N\tau} p_{rj} p_{rj}^* \quad (2.5)$$

We note that Eq. (2.5) differs from Eq. (2.4) by a multiplicative factor, $\frac{\pi}{4}$. Hence, in the coming discussion we only consider continuous wave detection systems. The discussion for pulsed systems could be managed in the same manner.

2.3 The bistatic case

Consider now the wave scattered from an ensemble of the scatterers in the bistatic case as shown in Fig. 2. The transmitting and receiving transducers (T and R in Fig. 2) are assumed to be circular, and to have equal and narrow beamwidths. The detected volume is the area where the narrow conical transmitter beam pattern and the receiving solid angle intersect. The incident path length is r_{ij} , r_{sj} is the scattered path length, r_s is the distance from transmitter (or receiver) to the center of the detected volume, and β_s is the half width of the main lobe of the directivity pattern (i.e. $2\beta_s$ is the angular separation of the -3 dB points).

In this case the incident pressure wave in Eq. (2.1) takes the form

$$p_i = (p_s r_s / r_i) \exp(-\bar{\alpha} r_i) D_i \exp[i(k r_i - \omega t)] \quad (2.6)$$

where r_s is the distance along the acoustic axis to the point at which the sound pressure level is p_s , D_i is the directivity of the transmitter, r_i is the distance from the transmitter to the particle, and $\bar{\alpha}$ is the attenuation coefficient, which is assumed to be uniform along the incident and scattered paths. (The overbar denotes the average over the particle size distribution.) As will be seen, this assumption is reasonable for the bistatic systems considered here because of the small distance involved. The scattered pressure from the j th scatterer is given by

$$p_{sj} = \frac{p_s r_s}{2r_{ij} r_{sj}} D_{ij} D_{sj} a_j f_{\infty}(\theta_j, a_j) \times \exp[-\bar{\alpha}(r_{ij} + r_{sj})] \exp[i(k(r_{ij} + r_{sj}) - \omega t)] \quad (2.7)$$

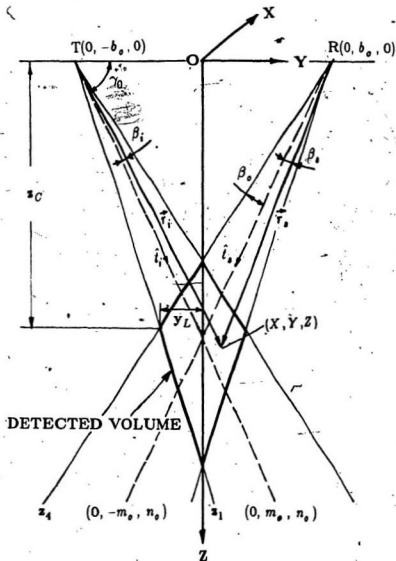


Figure 2. The geometry for the bistatic case. T is the transmitter, R is the receiver. The remaining symbols are defined in the text.

where D_i is the directivity of the receiver. For a system in which the same transducer is used both to transmit and receive (the monostatic case), the received pressure is called the backscattered pressure. In this case $D_{ij} = D_{ji}$, and $r_{ij} = r_{ji}$, so Eq. (2.7) becomes

$$p_{ij} = \frac{p_s r_s}{2r_i r_j} D_j^2 a_j f_{\infty}(\pi, a_j) \exp[-2\alpha r_j] \exp[i(2k r_j - \omega t)] \quad (2.8)$$

where we used $D_j = D_{ij} = D_{ji}$ and $r_j = r_{ij} = r_{ji}$.

In oceanographic applications, the particles will not be of uniform size. Let $n(a)$ be the size spectral density. For spherical particles, the mass concentration of suspended matter M is given by

$$M = N \rho'_s \frac{4}{3} \pi \int_0^{\infty} a^3 n(a) da \quad (2.9)$$

where ρ'_s is the grain density of each scatterer. Let $d\tau$ be the volume element, then the summation in Eq. (2.4) becomes an integral over the detected volume.

For an arbitrary size distribution, Eq. (2.4) can be rewritten as

$$\dot{p}_s^2 = \iiint_N \left[\int_0^{\infty} p_s p_s^* n(a) da \right] d\tau \quad (2.10)$$

Using Eqs. (2.7) and (2.9) in the above equation, we get

$$\dot{p}_s^2 = \frac{3Mp_s^2}{4\pi\rho_s'} \iiint \left\{ \frac{r_s^2}{4r_i^2 r_j^2} D_i^2 D_j^2 \exp[-2\alpha(r_i + r_j)] \frac{\int_0^{\infty} a^2 |f_{\infty}(\theta, a)|^2 n(a) da}{\int_0^{\infty} a^3 n(a) da} \right\} d\tau \quad (2.11)$$

We note from Fig. 2 that $\text{MIN}(\theta_j) = \theta_s - 2\beta_s$ and $\text{MAX}(\theta_j) = \theta_s + 2\beta_s$. Typical values of β_s considered here are $1 \sim 2^\circ$. The variation in scattering angle over the detected volume is therefore small, and we assume that $|f_\infty(\theta, a)|^2 = |f_\infty(\theta_s, a)|^2$. The validity of this assumption is tested later. If it is also assumed that $n(a)$ does not vary within the detected volume, then

$$\hat{p}_s^2 = p_s^2 G^2 H_s^2 \quad (2.12)$$

where

$$G^2 = \iiint \frac{r_s^2}{4r_i^2 r_s^2} D_i^2 D_s^2 \exp[-2\bar{\alpha}(r_i + r_s)] d\tau \quad (2.13)$$

and

$$H_s^2 = \frac{3MA^2}{4\pi\rho_s B^2} \quad (2.14)$$

where

$$A^2 = \int_0^\infty |f_\infty(\theta_s, a)|^2 a^2 n(a) da \quad (2.15)$$

and

$$B^2 = \int_0^\infty a^3 n(a) da \quad (2.16)$$

Equations (2.12) to (2.16) form the basis for discussion in the rest of this thesis. Note that while A and B depend only on $n(a)$, G^2 depends on both $n(a)$ and M through the linear attenuation coefficient $\bar{\alpha}$. We wish to obtain an

approximate analytic expression for G^2 , valid in the narrow beam case. It appears however that this problem has not always been treated properly in the literature. For this reason, and because a useful approximate solution is introduced, the problem is considered in detail in the following Section.

2.4 The detected volume τ and G^2 for bistatic systems

In order to evaluate G^2 (Eq. 2.13), we must first obtain approximate expressions for each of the terms in the integrand for the narrow beam case.

Suppose that the transmitter and the receiver are both on the Y -axis, and that their acoustic axes lie in the YZ -plane (see Fig. 2). Then the coordinates of each transducer are $(0, -b_s, 0)$ and $(0, b_s, 0)$, respectively, and the direction cosines of the main beam axes are $(0, m_s, n_s)$ for the transmitter and $(0, -m_s, n_s)$ for the receiver. We have

$$b_s = r_s m_s, \quad m_s = \cos \gamma_s, \quad n_s = \sin \gamma_s \quad (2.17)$$

where $\gamma_s = \frac{\theta_s}{2}$.

Consider the main lobes of the transducer beam patterns to be cones with their apex at the center of each transducer. Let \hat{i}_t and \hat{i}_r be unit vectors along the axes of the transmitter and receiver cones, respectively. That is

$$\hat{i}_t = m_s \hat{j} + n_s \hat{k} \quad (2.18)$$

and

$$\mathbf{i}_s = -m_s \mathbf{j} + n_s \mathbf{k} \quad (2.19)$$

Let (X, Y, Z) be the coordinates of a particle which is located in the detected volume. Then let \mathbf{r}_i be the distance vector lying on the straight line connecting the apex of the transmitter cone and (X, Y, Z) , and \mathbf{r}_r a vector lying on the straight line connecting the apex of the receiver cone and (X, Y, Z) (see Fig. 2). Then

$$\mathbf{r}_i = X\mathbf{i} + (Y + b_s)\mathbf{j} + Z\mathbf{k} \quad (2.20a)$$

$$\mathbf{r}_r = X\mathbf{i} + (Y - b_r)\mathbf{j} + Z\mathbf{k} \quad (2.20b)$$

We consider the directivity terms in Eq. (2.13) first. For a circular transducer of radius a_s uniformly sensitive over its surface, the directivity D takes the form [Clay and Medwin, 1977, p. 144]

$$D = \frac{2J_1(k_s a_s \beta)}{k_s a_s \beta} = \frac{2J_1(\xi)}{\xi} \quad (2.21)$$

where β is the angle with respect to the acoustic axis, J_1 is the order 1 Bessel function of the first kind, and $\xi = k_s a_s \beta$. Eq. (2.21) holds in the far field: that is, for $r_{si}, r_{sj} \geq \pi a_s^2 / \lambda$ [Clay and Medwin, 1977, p. 155].

We choose β_s to be at the -3 dB points ($D^2 = \frac{1}{2}$) of the main lobe of the beam pattern; that is, at $\xi_s = k_s a_s \beta_s \approx 1.6$. We therefore consider the directivity only in the range $0 \leq \xi \leq \xi_s$. From Abramowitz and Stegun [1968, p.370], for $-3.0 \leq \xi \leq 3.0$, we can use

$$\frac{2J_1(\xi)}{\xi} \approx 1 - 1.124 \left(\frac{\xi}{3} \right)^2 \quad (2.22)$$

The maximum error introduced by this approximation occurs at $\xi = \xi_0$, and is about 5%. Therefore D in Eq. (2.21) takes the form

$$D \approx 1 - 1.124 \left(\frac{\xi}{3} \right)^2 = 1 - \frac{(k_c a_0 \beta)^2}{8} \quad (2.23)$$

Ignoring terms of order $\frac{(k_c a_0 \beta)^4}{64}$, we get

$$D_i^2 D_s^2 \approx 1 - \frac{1}{4} (k_c a_0)^2 [\beta_i^2 + \beta_s^2] \quad (2.24)$$

From Eqs. (2.18), (2.19) and (2.20), we have

$$\hat{i}_i \cdot \vec{r}_i = r_i \cos \beta_i = m_0 (Y + b_0) + n_0 Z \quad (2.25a)$$

$$\hat{i}_s \cdot \vec{r}_s = r_s \cos \beta_s = -m_0 (Y - b_0) + n_0 Z \quad (2.25b)$$

and

$$|\hat{i}_i \times \vec{r}_i| = r_i \sin \beta_i = [m_0 Z - n_0 (Y + b_0)] \hat{i} + n_0 X \hat{j} - m_0 X \hat{k} \quad (2.26a)$$

$$|\hat{i}_s \times \vec{r}_s| = r_s \sin \beta_s = [-m_0 Z - n_0 (Y - b_0)] \hat{i} + n_0 X \hat{j} + m_0 X \hat{k} \quad (2.26b)$$

where β_i is the angle between \hat{i}_i and \vec{r}_i and β_s is the angle between \hat{i}_s and \vec{r}_s (see Fig. 2).

Making the following change of variable

$$\zeta = Z - Z_0 = Z - r_s n_0 \quad (2.27)$$

Eq. (2.26) can be rewritten as

$$r_i \sin \beta_i = \left| (m_o \zeta - n_o Y) i + n_o X j - m_o X k \right| \quad (2.28a)$$

$$r_o \sin \beta_o = \left| (-m_o \zeta - n_o Y) i + n_o X j + m_o X k \right| \quad (2.28b)$$

For the narrow beam case, $\cos \beta_i \approx \cos \beta_o \approx 1$, and from Eq. (2.25) we have

$$r_i + r_o \approx 2r_o \left[1 + \frac{n_o \zeta}{r_o} \right] \quad (2.29)$$

Since $\sin^2 \beta \approx \beta^2$, squaring Eq. (2.26) gives

$$\beta_i^2 + \beta_o^2 = \frac{(m_o \zeta - n_o Y)^2 + X^2}{r_i^2} + \frac{(m_o \zeta + n_o Y)^2 + X^2}{r_o^2} \quad (2.30)$$

From Eq. (2.25a) we have

$$r_i^2 = [m_o(Y + m_o r_o) + n_o(n_o r_o + \zeta)]^2 = r_o^2 \left[1 + \frac{(m_o Y + n_o \zeta)}{r_o} \right]^2$$

or, since $\frac{m_o Y + n_o \zeta}{r_o} \ll 1$,

$$r_i^2 \approx r_o^2 \left[1 + \frac{2(m_o Y + n_o \zeta)}{r_o} \right]$$

and

$$\frac{1}{r_i^2} \approx \frac{1}{r_o^2} \left[1 - \frac{2}{r_o} (m_o Y + n_o \zeta) \right] \quad (2.31)$$

Similarly,

$$r_o^2 \approx r_o^2 \left[1 + \frac{2(-m_o Y + n_o \zeta)}{r_o} \right]$$

and

$$\frac{1}{r_o^2} \approx \frac{1}{r_o^2} \left[1 - \frac{2}{r_o^2} (-m_o Y + n_o \zeta) \right] \quad (2.32)$$

Using Eqs. (2.31) and (2.32) in Eq. (2.30), we get

$$\beta_i^2 + \beta_o^2 = \frac{2}{r_o^2} \left[X^2 + n_o^2 Y^2 + m_o^2 \zeta^2 \right] \quad (2.33)$$

Substituting the above equation into Eq. (2.3), we finally get

$$D_i^2 D_o^2 \approx 1 - \frac{(k_c a_o)^2}{2r_o^2} \left[X^2 + n_o^2 Y^2 + m_o^2 \zeta^2 \right] \quad (2.34)$$

The attenuation coefficient in Eq. (2.13) can be separated into terms due to the ambient fluid, α_o , and due to the scatterers, $\bar{\alpha}_s$ (we ignore the attenuation due to viscous damping and thermal conductivity, which will be discussed in Chapter 4). In freshwater α_o can be written as [Clay and Medwin, 1977, p. 98]

$$\alpha_o = \frac{163.44 f^2 \left(\frac{4}{3} \mu_F + \mu_F' \right)}{\rho_o c^3} \quad (2.35)$$

where f is the acoustic frequency, μ_F is the dynamic coefficient of shear viscosity for freshwater, and μ_F' is the dynamic coefficient of bulk viscosity for freshwater.

The attenuation coefficient $\bar{\alpha}_s$ is a complex function of size and frequency. For frequencies such that the acoustic wavelength is much less than the scatter circumference, however, $\bar{\alpha}_s$ is given by (see Chapter 4 or Morse and Ingard, 1968, p. 419),

$$\bar{\alpha}_s = \frac{3}{4} \frac{\epsilon}{\bar{\alpha}} = \frac{3M}{4\bar{\alpha}\rho_s} \quad (2.36)$$

In the cases of interest here, the frequency is in the range $0.5 \text{ MHz} \leq f \leq 10 \text{ MHz}$, the concentration of the scatterers less than 10 kg m^{-3} , and the average radius of the scatterers is in the range of $30 \text{ } \mu\text{m} < \bar{r} < 300 \text{ } \mu\text{m}$. Suppose $T = 15^\circ \text{C}$, so that $c = 1466 \text{ m s}^{-1}$, $\rho_s = 999.1 \text{ kg m}^{-3}$, $\mu_F \approx 1.19 \text{ N s m}^{-3}$ and $\mu_F' \approx 3.30 \text{ N s m}^{-2}$. In this situation we have $\alpha_s \leq 2.660 \text{ m}^{-1}$ and $\bar{\alpha}_s < 5.66 \text{ m}^{-1}$, such that

$$\bar{\alpha} = \alpha_s + \bar{\alpha}_s < 8.320 \text{ m}^{-1} \quad (2.37)$$

Now, using Eq. (2.29), the exponential in Eq. (2.13) becomes

$$\exp \left[-4\bar{\alpha}r_s - 4\bar{\alpha}n_s \zeta \right]$$

Because

$$\zeta_{\max} \approx \frac{r_s \beta_s}{\cos \gamma_s} \quad (2.38)$$

we therefore have, using Eq. (2.37)

$$4\bar{\alpha}n_s \zeta < 4r_s \beta_s \tan \gamma_s (\alpha_s + \bar{\alpha}_s) < 5 \beta_s \tan \gamma_s \quad (2.39)$$

for $r_s = 0.15 \text{ m}$, which is typical of the systems considered here.

For $\gamma_s \leq 75^\circ$ and $\beta_s \leq 2^\circ$, therefore $2\bar{\alpha}n_s \zeta \ll 1$, and Eq. (2.13) can be written as

$$G^2 = \frac{r_s^2 e^{-4\bar{\alpha}r_s}}{4r_s^4} \iiint \left[1 - \frac{2}{r_s} (-m_s Y + n_s \zeta) \right] \left[1 - \frac{2}{r_s} (m_s Y + n_s \zeta) \right] \\ \times \left[1 - \frac{(k_s a_s)^2}{2r_s^2} [X^2 + n_s^2 Y^2 + m_s^2 \zeta^2] \right] (1 - 4\bar{\alpha}n_s \zeta) d\tau$$

where Eqs. (2.32) and (2.34) have been used.

Ignoring higher order terms as before, we have

$$G^2 = \frac{\tau r_o^2 e^{-4\bar{\alpha} r_o}}{4r_o^4} \times \left\{ 1 - \frac{1}{\tau} \iiint \left[\frac{4n_o \zeta}{r_o} + 4\bar{\alpha} n_o \zeta + \frac{(k_c a_o)^2 (X^2 + n_o^2 Y^2 + m_o^2 \zeta^2)}{2r_o^2} \right] d\tau \right\} \quad (2.40)$$

2.4.1 Numerical evaluation of τ and G^2

Booker and Bettencourt [1955] appear to have been the first to estimate the value of τ , and detailed consideration of this problem was given by Sugai [1965]. We have not found any subsequent derivations of τ in the literature. Since there are two errors in Sugai's derivation, the problem is considered in detail below.

For the transmitter cone, let $\beta_i = \beta_o$ in Eq. (2.25a), we get

$$m_o (Y + b_o) + n_o Z = r_i \cos \beta_o \quad (2.41)$$

where

$$r_i^2 = X^2 + (Y + b_o)^2 + Z^2 \quad (2.42)$$

which are equivalent to Eq. (1) in Sugai [1965].

Similarly for the receiver cone, with apex at $(0, b_o, 0)$ and $\beta_r = \beta_o$, we have

$$-m_o (Y - b_o) + n_o Z = r_r \cos \beta_o \quad (2.43)$$

and

$$r_s^2 = X^2 + (Y - b_s)^2 + Z^2 \quad (2.44)$$

Following Sugai [1965], let Z_1 represent the lower half surface of the transmitter cone and Z_4 represent the upper half surface of the receiver cone. From Eqs. (2.41) and (2.43) we have

$$Z_1 = C_s(Y + b_s) + A_s \sqrt{B_s^2(Y + b_s)^2 - X^2} \quad (2.45a)$$

$$Z_4 = -C_s(Y - b_s) - A_s \sqrt{B_s^2(Y - b_s)^2 - X^2} \quad (2.45d)$$

where

$$\begin{cases} A_s \sqrt{1 - n_o^2 \sec^2 \beta_s} = 1 \\ B_s = A_s \tan \beta_s \\ C_s = A_s^2 m_s n_o \sec^2 \beta_s \end{cases} \quad (2.46)$$

From Eq. (2.45) with $Z_1 = Z_4 = Z_c$ and $X = 0$, we get

$$Z_C = \frac{b_s}{m_s n_o} (\cos^2 \beta_s - m_o^2) \quad (2.47)$$

where Z_C is defined by the point of intersection of Z_4 with Z_1 (Fig. 2) in the $X=0$ plane. The intersections of the transmitter and receiver cones with the $Z = Z_C$ plane are ellipses which overlap exactly. We note that in general the point $(0; 0, Z_c)$ (Fig. 2) will not coincide with the intersection point of the acoustic axes of the two transducers.

From any one of Eq. (2.45) with $Z = Z_C$ and $X = 0$ we find

$$K = \frac{b_s A_s B_s}{C_s} \quad (2.48)$$

For very narrow beamwidths (for example $\beta_s < 2^\circ$), we drop terms $O(\beta_s^2)$ relative to 1, and Eqs. (2.47) and (2.48) can be approximated by

$$\begin{cases} Z_C \approx r_s n_s \\ Y_L \approx \frac{r_s \beta_s}{n_s} \end{cases} \quad (2.49)$$

and the ellipses in the $Z = Z_C$ plane can be approximately expressed by

$$\frac{n_s^2 Y^2}{r_s^2 \beta_s^2} + \frac{X^2}{r_s^2 \beta_s^2} = 1 \quad (2.50)$$

Since the detected volume is symmetric about the planes of $Y = 0$ and $X = 0$, we have

$$\tau = 4 \int_{-Y_L}^0 dY \int_0^w dX \int_{Z_C}^{Z_1} dZ \quad (2.51)$$

where w is the width of the ellipse in the X direction. From Eq. (2.50), w is

$$w = \sqrt{r_s^2 \beta_s^2 - n_s^2 Y^2} \quad (2.52)$$

Sugai [1965] mistakenly took w to be a linear function of Y . Sugai's range of integration in the Y direction is also incorrect.

As shown in Appendix A, after integrating with respect to X , the resultant integration with respect to Y must be carried out numerically. For the parameter range $10 \text{ cm} \leq r_s \leq 60 \text{ cm}$, $10^\circ \leq \gamma_s \leq 80^\circ$ and $0.5^\circ \leq \beta_s \leq 3^\circ$, the result is

$$\tau = (5.1 \sim 5.2) \frac{r_o^3 \beta_o^3}{\sin \theta_o} \quad (2.53)$$

These results for τ are to be compared with Sugai's result $\tau = 4\pi \frac{r_o^3 \beta_o^3}{\sin \theta_o}$, which is

large, and Booker and Bettenourt's result $\tau = 2 \frac{r_o^3 \beta_o^3}{\sin \theta_o}$, which is small.

The evaluation of G^2 can proceed in the same manner. Let

$$g(X, Y, \zeta) = \left[4\bar{\alpha} n_o \zeta + \frac{4n_o \zeta}{r_o} + \frac{(k_o a_o)^2}{2r_o^2} (X^2 + n_o^2 Y^2 + m_o^2 \zeta^2) \right] \quad (2.54)$$

then Eq. (2.40) can be written as

$$G^2 = \frac{\tau r_o^2 e^{-4\bar{\alpha} r_o}}{4r_o^4} \left[1 - \frac{1}{\tau} \iiint g(X, Y, \zeta) d\tau \right] \quad (2.55)$$

where

$$\frac{1}{\tau} \iiint g(X, Y, \zeta) d\tau = \frac{2}{\tau} \int_{-Y_1}^0 dY \int_{-X_1}^X dX \int_{\zeta_1}^{\zeta_2} g(X, Y, \zeta) d\zeta \quad (2.56)$$

with $\zeta_1 = Z_1 - Z_C$ and $\zeta_2 = Z_2 - Z_C$.

The numerical integration of the above equation is given in Appendix A for the parameter range $20^\circ \leq \gamma_o \leq 70^\circ$, $5 \text{ cm} \leq r_o \leq 50 \text{ cm}$ and $0.01^\circ \leq \beta_o \leq 3^\circ$. Some numerical results are shown in Table 1.

Table 1. The numerical values of G^2/r_s^2 and the comparison with results of the parabolic approximation.

r_s cm	γ_s degrees	β_s degrees	numerical value	parabolic approximation	discrepancy %
15	30	0.1	0.6119	0.5550	9.3
		0.5	0.6121	0.5549	9.3
		1.0	0.6127	0.5544	9.5
		2.0	0.6152	0.5524	9.5
		3.0	0.6198	0.5490	11.4
15	45	0.1	0.6119	0.5550	9.3
		0.5	0.6119	0.5548	9.3
		1.0	0.6118	0.5540	9.4
		2.0	0.6116	0.5482	10.4
		3.0	0.6114	0.5460	10.7
15	60	0.1	0.6119	0.5550	9.3
		0.5	0.6116	0.5545	9.3
		1.0	0.6108	0.5530	9.5
		2.0	0.6078	0.5414	10.9
		3.0	0.5855	0.5271	10.0

2.4.2 Parabolic approximation for τ and G^2

We note that the cross-section of the common volume in the XZ -plane is the intersection of two ellipses of which the centers do not coincide except in the $Y = 0$ plane (Fig. 3). We use two parabolas to approximate part of each ellipse within the detected volume. We define this kind of approximation as the "parabolic approximation". The detected volume now becomes

$$\tau = 4 \int_{-Y_1}^0 dY \int_0^{Z_1} dX \int_{Z_1}^{Z_2} dZ \quad (2.57)$$

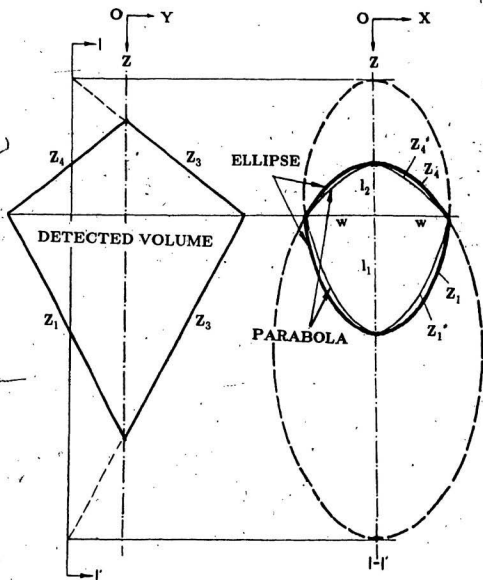


Figure 3. Parabolic approximation of the cross-section in XZ -plane. Π' represents a plane parallel to the XZ -plane, and the ellipses shown are in the Π' plane.

The parameters Z_1' and Z_4' in the above equation are the parabolic approximations to the lower and upper surfaces of the left side of the detected volume and are given by

$$Z_1' = n_s r_s + l_1 \left(1 - \frac{X^2}{w^2} \right) \quad (2.58)$$

$$Z_4' = n_s r_s + l_2 \left(\frac{X^2}{w^2} - 1 \right) \quad (2.59)$$

where l_1 and l_2 (refer to Fig. 3) are obtained from Eqs. (2.45) with $X = 0$. That is,

$$l_1 = Z_1 - Z_C = \frac{(m_s n_s + \beta_s) Y + m_s r_s \beta_s}{m_s^2} \quad (2.60)$$

and

$$l_2 = Z_C - Z_4 = \frac{(m_s n_s - \beta_s) Y + m_s r_s \beta_s}{m_s^2} \quad (2.61)$$

Therefore we have

$$\tau = \int_{-Y_1}^0 \frac{16(n_s Y + r_s \beta_s) \sqrt{r_s^2 \beta_s^2 - n_s^2 Y^2}}{3m_s} dY$$

Integrating with respect to Y and using $2n_s m_s = \sin 2\gamma_s = \sin \theta_s$, finally we have

$$\tau = \frac{24\pi - 32}{9} \frac{r_s^3 \beta_s^3}{2n_s m_s} = 4.822 \frac{r_s^3 \beta_s^3}{\sin \theta_s} \quad (2.62)$$

This result is within 8% of our numerical value given in Eq. (2.54).

We also introduce the "parabolic approximation" to the integral of Eq. (2.56). In the parabolic approximation ζ_1 and ζ_2 in Eq. (2.56) take the forms

$$\zeta_1 = Z_1' - n_o r_o = l_1 \left[1 - \frac{X^2}{w^2} \right] \quad (2.63)$$

and

$$\zeta_2 = Z_2' - n_o r_o = l_2 \left[\frac{X^2}{w^2} - 1 \right] \quad (2.64)$$

where w , Z_1' , Z_2' , l_1 and l_2 have been given in Eqs. (2.52), (2.58) to (2.61).

Integrating Eq. (2.56) with respect to ζ , we have

$$\begin{aligned} \frac{1}{\tau} \iiint g d\tau = & \frac{1}{\tau} \int_{-Y_1}^0 dY \int_{-\frac{w}{3r_o}}^0 \frac{1}{3r_o^2} \left[(k_c a_o)^2 m_o^2 (\zeta_1^3 - \zeta_2^3) \right. \\ & \left. + 12n_o r_o (\bar{\alpha} r_o + 1)(\zeta_1^2 - \zeta_2^2) + 3[(k_c a_o)^2 n_o^2 Y^2 + (k_c a_o)^2 X^2](\zeta_1 - \zeta_2) \right] dX \quad (2.65) \end{aligned}$$

Integrating the above equation with respect to X , we have

$$\begin{aligned} \frac{1}{\tau} \iiint g d\tau = & \frac{1}{105 m_o^3 r_o^2 \tau} \left\{ 8(k_c a_o)^4 n_o \int_{-Y_1}^0 w Y^3 (24\beta_o^2 + 43m_o^2 n_o^2) dY \right. \\ & + 8r_o \int_{-Y_1}^0 w Y^2 [28(k_c a_o)^2 \beta_o^3 + 224\bar{\alpha} n_o^2 \beta_o r_o \\ & \left. + 50(k_c a_o)^2 n_o^2 m_o^2 \beta_o + 224n_o^2 \beta_o] dY \right\} \end{aligned}$$

$$\begin{aligned}
& + 8 \int_{-Y_1}^Y w Y [7(k_c a_s)^2 m_s^2 n_s w^2 + 224 \bar{\alpha} n_s r_s^2 \beta_s^2 \\
& + 24(k_c a_s)^2 m_s^2 n_s r_s^2 \beta_s^2 + 224 n_s r_s^2 \beta_s^2] dY \\
& + 8(k_c a_s)^2 m_s^2 r_s \beta_s \int_{-Y_1}^Y w [7w^2 + 8r_s^2 \beta_s^2] dY \Bigg\}
\end{aligned}$$

Integrating the above equation with respect to Y , we get

$$\frac{1}{r} \iint g d\tau = 0.2168 (k_c a_s)^2 \beta_s^2 - \frac{0.970 \beta_s^2 (\bar{\alpha} r_s + 1)}{\cos^2 \gamma_s} \quad (2.66)$$

Eq. (2.66) is within 10% of the numerical values of Eq. (2.56) in the parameter range considered before. The comparison is shown in Table 1.

Using Eq. (2.66) in Eq. (2.55), G^2 takes the form

$$G^2 = \frac{\tau r_s^2 e^{-45r_s}}{4r_s^4} \left[1 + \frac{0.970 \beta_s^2 (\bar{\alpha} r_s + 1)}{\cos^2 \gamma_s} - 0.2168 (k_c a_s)^2 \beta_s^2 \right] \quad (2.67)$$

For the terms enclosed by square brackets in Eq. (2.67), we use the same parameters as before and let the radius of the transducer $a_s = 2.5$ mm (this is typical of the bistatic systems considered here), and $\bar{\alpha} = 8.320 \text{ m}^{-1}$. So that we have $\bar{\alpha} r_s = 1.248$ and with $k_c a_s \beta_s \approx 1.8$, the terms in square brackets become

$$[1 + 0.01038 - 0.5550] \quad (2.68)$$

We note that the second term in the above square bracket is small relative to the

first and last terms, so we have

$$G^2 = \frac{G_o^2 \tau r_o^2 \exp[-4\alpha_o r_o]}{4r_o^4} \quad (2.69)$$

where $G_o^2 = 0.45$. Eq. (2.12) may therefore be rewritten in the form

$$\dot{p}_o^2 = S^2 H_o^2 \exp[-4\alpha_p r_o] \quad (2.70)$$

where

$$S^2 = \frac{p_o^2 \tau r_o^2}{4r_o^4} G_o^2 \exp[-4\alpha_o r_o] \quad (2.71)$$

and where α_p is the additional attenuation due to the particles, and α_o has the same definition as before.

2.5 Multiple scattering limit

In the previous discussion we considered low particle concentrations: that is, we ignored multiple scattering. In this section we shall estimate the concentration at which multiple scattering becomes important. For simplicity, we initially assume isotropic scattering (the form factor is independent of scattering angle), and we consider the particles to be of uniform size.

Choose two scatterers, the j th and the k th scatterer, and suppose the scattered pressure from the j th particle will be rescattered by the k th scatterer. Referring to Fig. 4, the distance from the j th particle to the transmitter is r_{ij}

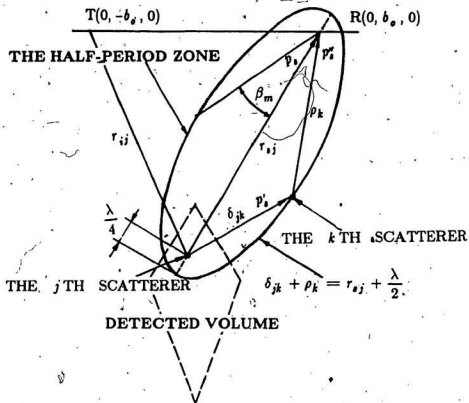


Figure 4. The half-period zone for the first order multiple scattered waves.

and to the receiver is r_{sj} , respectively, which are the same definitions as in Section 2.1. The distance from the k th particle to j th particle is δ_{jk} and to the receiver is ρ_k , respectively.

Following Waterman and Truell [1961], the Fresnel half-period zones are ellipsoids, and the interior of the n th half-period zone is defined by $r_{sj} + (n-1)\frac{\lambda}{2} \leq \delta_{jk} + \rho_k \leq r_{sj} + n\frac{\lambda}{2}$, where n is an integer and λ is the acoustic wavelength. In each zone all waves rescattered by particles which are located in this zone have amplitudes of the same sign when they arrive at R. On average the contributions from adjacent zones will be opposite in sign, and because of the attenuation and radial spreading of the scattered wave from the j th particle, we can say the total contribution from several zones could not be bigger than the contribution from the first zone. As a result we only need to consider the multiple scattering from the first zone, the boundary of which is defined by $\delta_{jk} + \rho_k = r_{sj} + \frac{\lambda}{2}$ (see Fig. 4). The scattered and rescattered pressures are given by

$$p_{sj} = p_i \left[\frac{af_{\infty}}{2r_{sj}} \right] \exp[ik_c r_{sj}] \quad (2.72a)$$

$$p'_{sj} = p_i \left[\frac{af_{\infty}}{2\delta_{jk}} \right] \exp[ik_c \delta_{jk}] \quad (2.72b)$$

$$p''_{sj} = p_i \left[\frac{a^2 f_{\infty}^2}{4\rho_k \delta_{jk}} \right] \exp[ik_c (\delta_{jk} + \rho_k)] \quad (2.72c)$$

where p_{sj} and p'_{sj} are the scattered pressure from the j th particle at the dis-

tances r_{sj} and δ_{sj} , respectively, and p_{sj}^* is the multiple scattered pressure (the first order) at R.

Let P_{1j} be the total multiple scattered pressure of the first order in the first Fresnel half-period-zone, so that we have

$$P_{1j} = N \iiint_{\text{zone 1}} p_{sj}^* d\tau \quad (2.73)$$

Substituting Eq. (2.72c) into Eq. (2.73), we have

$$P_{1j} = \frac{1}{4} p_i a^2 f^2 N \iiint_{\text{zone 1}} \left[\frac{1}{\delta \rho} \exp[ik_c(\delta + \rho)] \right] d\tau \quad (2.74)$$

where the subscripts on δ and ρ have been dropped for convenience.

Following Waterman and Truell [1961], we choose bipolar coordinates ρ , δ , and Φ (the azimuthal angle about the acoustic axis) for the integration. In the first zone we have

$$r_{sj} \leq \delta + \rho \leq r_{sj} + \frac{\lambda}{2} \quad (2.75)$$

and

$$\begin{cases} 0 \leq \rho \leq r_{sj} + \frac{\lambda}{4} \\ 0 \leq \Phi \leq 2\pi \end{cases} \quad (2.76)$$

The volume element is [Reed and Gunnins, 1973, pp.458-459]

$$d\tau = \frac{\delta \rho}{r_{sj}} d\rho d\delta d\Phi \quad (2.77)$$

so that

$$P_{1j} = \frac{1}{4} p_i a^2 f_{\infty} N \int_0^{2\pi} d\Phi \int_0^{\frac{r_{ij} + \frac{\lambda}{4}}{r_{ij} - \rho + \lambda/2}} d\rho \int_{r_{ij} - \rho}^{\frac{1}{r_{ij}}} \exp[ik_c(\delta + \rho)] d\delta$$

After integration we get

$$P_{1j} = \left[\frac{\pi i a f_{\infty} N (r_{sj} + \frac{\lambda}{4})}{k_c} \right] p_i \frac{a f_{\infty}}{r_{sj}} \exp[ik_c r_{sj}] \quad (2.78)$$

which can be written as

$$\frac{P_{1j}}{p_{sj}} = \frac{2\pi i a f_{\infty} N r_{sj}}{k_c}$$

since $\frac{\lambda}{4} \ll r_{sj}$. For the narrow beam case we have $r_{sj} \approx r_o$, and the above equation becomes

$$\frac{P_{1j}}{p_{sj}} = \frac{2\pi i a f_{\infty} N r_o}{k_c} \quad (2.79)$$

If $\left| \frac{P_1}{p_s} \right| \ll 1$, then multiple scattering can be ignored. This condition holds if

$$N \ll \frac{k_c}{2\pi a |f_{\infty}| r_o} \quad (2.80)$$

Since

$$\frac{M}{\rho_o} = \frac{4}{3} \pi a^3 N$$

for uniformly sized scatterers, the condition (2.80) becomes

$$\frac{M}{\rho_s} \ll \frac{2k_e a^2}{3|f_\infty| r_s} \quad (2.81)$$

Let us consider cases in which $k_e a \ll 1$, $a \sim 50 \mu\text{m}$, $|f_\infty| \sim (k_e a)^2$ (see Chapter 3, or Rayleigh 1945, p. 283) and $r_s \approx 0.1 \text{ m}$. We get

$$\frac{M}{\rho_s} \ll 5 \times 10^{-3} \quad (2.82)$$

For quartz particles, $\rho_s \sim 3 \times 10^3 \text{ kg/m}^3$, giving $M \ll 15 \text{ kg/m}^3$.

The condition (2.81) is, however, too restrictive because the transducer directivity has not been considered. From Fig. 4 we can show that β_m , the angle subtended by half the minor axis of the first zone, is given by

$$\cos \beta_m = \frac{r_{sj}/2}{r_{sj}/2 + \lambda/4} \approx 1 - \frac{\lambda}{2r_{sj}} \quad (2.83)$$

and since $r_{sj} \approx r_s$,

$$\beta_m \approx \sqrt{\frac{\lambda}{r_s}} = \sqrt{\frac{c}{r_s f}} \quad (2.84)$$

Considering a typical case where $r_s = 0.15 \text{ m}$, $f = 8 \text{ MHz}$, $\beta_s = 1^\circ$, and the speed of the sound $c = 1500 \text{ m s}^{-1}$, we get $\beta_m \approx 2^\circ$. Therefore

$$\beta_m \approx 2 \beta_s \quad (2.85)$$

From Eq. (2.85) we note that most of the receiver cone is inside the first Fresnel zone. Since the receiver is sensitive primarily to the scattered waves from the par-

ticles which are located in the receiver cone, therefore the total multiple scattered pressure calculated by Eq. (2.73) is bigger than that actually sensed by the receiver. In other words the actual value of maximum concentration for ignoring the multiple scattering could be bigger than that estimated from Eq. (2.81).

The results obtained above require that $k_c a$ should be small so that the form factor is independent of scattering angle. For large values $k_c a$, the isotropic assumption does not hold, and for $k_c a$ large enough $|f_\infty|$ in the forward direction ($\theta = 0$) becomes very large (see Chapter 3, or Morse and Feshbach 1953, p. 1554). This permits us to consider multiple scattering only in this direction. The rescattered pressure in Eq. (2.72c) now takes the form

$$p_{sj}'' = p_i \left[\frac{4a^2 f_\infty(\theta) f_\infty(0)}{\rho_k \delta_k} \right] \exp[ik_c (\delta_{jk} + \rho_k)] \quad (2.86)$$

Since $\delta_{jk} + \rho_k = r_{sj}$, so that the total multiple scattered pressure of the first order in the forward direction P_{1j} is given by

$$P_{1j} = \frac{p_i a^2 f_\infty(\theta) f_\infty(0)}{4} \exp[ik_c r_{sj}] \sum_{k=1} \frac{1}{\delta_{jk} (r_{sj} - \delta_{jk})} \quad (2.87)$$

Let Δ be the average interval between any two neighboring particles. Clearly, Δ is equal to $1/N^{\frac{1}{3}}$. Then Eq. (2.87) becomes

$$P_{1j} = \frac{p_i a^2 f_\infty(\theta) f_\infty(0)}{4} \exp[ik_c r_{sj}] \int_{\Delta}^{r_{sj}-\Delta} \frac{1}{\delta(r_{sj}-\delta)} \frac{d\delta}{\Delta} \quad (2.88)$$

After integrating Eq. (2.88), we get

$$P_{1j} = \frac{N^{\frac{1}{3}} f_{\infty}(0) a}{4\Delta} \left[\frac{p_i a f_{\infty}(\theta) \exp[ik_c r_{sj}]}{2r_j} \right] \left[2 \log \frac{r_{sj}}{\Delta} \right] \quad (2.89)$$

if

$$\frac{P_{1j}}{P_{sj}} = N^{\frac{1}{3}} f_{\infty}(0) a \log[N^{\frac{1}{3}} r_{sj}] \quad (2.90)$$

If $\left| \frac{P_{1j}}{P_{sj}} \right| \ll 1$, multiple scattering can be ignored. Considering a typical case

with the uniform-sized scatterers of radius $a = 300 \mu\text{m}$ and $|f_{\infty}(0)| = 10$.

With $r_s = 0.15 \text{ m}$, we get $M \ll 2.0 \text{ kg m}^{-3}$. When the concentration is in this range, multiple scattering is negligible. It can be seen that when the amplitude of the forward scattered wave is large, the maximum concentration for ignoring multiple scattering will be smaller.

CHAPTER 3 THE FORM FACTOR

The theoretical computation of the form factor $|f_{\infty}|$ is made by using the partial wave phase shift formalism to obtain the scattered pressure field. In this chapter, $|f_{\infty}|$ is computed for the elastic sphere, the rigid-movable sphere and rigid-immovable sphere. The latter two are special cases of the first. The chapter begins with a brief presentation of the phase shift formalism, and numerical results for $|f_{\infty}|$ are presented in Section 3.2. A smooth analytic function which approximates the average form of $|f_{\infty}|$ is introduced in Section 3.3. The variation of $|f_{\infty}|$ with scattering angle is discussed in Section 3.4.

3.1 Phase shift formalism

Referring to Faran [1951], Hickling [1962] and Hay and Mercer [1985], the wave scattered by a solid elastic sphere is expressed as a sum of partial scattered waves in the form

$$p_s = p_i \exp(ik_c r) \sum_{n=0}^{\infty} (2n+1) i \sin \eta_n e^{-i\eta_n} P_n(\cos \theta) / k_c r \quad (3.1)$$

where the $\exp(-i\omega t)$ dependence has been dropped for convenience, and η_n is the phase shift of the n th partial wave, which is given by

$$\tan \eta_n = \tan \delta_n(x) \frac{[\tan \alpha_n(x) + \tan \Phi_n(x', s')]}{[\tan \beta_n(x) + \tan \Phi_n(x', s')]} \quad (3.2)$$

where

$$\tan \Phi_n = \frac{\frac{\rho_s s'^2}{2\rho_s'} \left[\frac{\tan \alpha_n(x')}{\tan \alpha_n(x') + 1} \frac{n^2 + n}{(n^2 + n - 1) - s'^2/2 + \tan \alpha_n(s')} \right]}{\left[\frac{n^2 + n - s'^2/2 + 2 \tan \alpha_n(x')}{\tan \alpha_n(x') + 1} \frac{(n^2 + n)(\tan \alpha_n(s') + 1)}{(n^2 + n - 1) - s'^2/2 + \tan \alpha_n(s')} \right]} \quad (3.3)$$

with

$$\tan \delta_n(x) = - \frac{j_n(x)}{n_n(x)} \quad (3.4a)$$

$$\tan \alpha_n(x) = - \frac{x j_n'(x)}{j_n(x)} \quad (3.4b)$$

$$\tan \beta_n(x) = - \frac{x n_n'(x)}{n_n(x)} \quad (3.4c)$$

where $j_n(x)$ and $n_n(x)$ are the spherical Bessel functions of the first and the second kinds, respectively. The primes on the Bessel functions denote the derivative with respect to the argument. Otherwise primes denote properties of the scatterer. The distance from the sphere to an arbitrary field point $P(r, \phi, \theta)$ is r , ρ_s' is the density of the particle, ρ_s is the density of the fluid; $x = k_c a$, $x' = k_c' a$, and $s' = k_s' a$. Here k_c' and k_s' are respectively the wavenumbers of the compression and shear waves in the scatterer, which can be written as

$$k_c' = \omega/c_p', \quad k_s' = \omega/c_s'$$

c_p' and c_s' being the compression and shear wave phase speeds in the scatterer,

respectively, given by

$$c_p'^2 = (\lambda' + 2\mu')/\rho_o', \quad c_s' = \mu'/\rho_o'$$

where λ' and μ' are the Lamé constants of the scatterer.

Eq. (3.1) can be written as [Morse and Feshbach, 1953, p.1573],

$$\begin{aligned} p_s &= \frac{p_o a}{2r} \left[\frac{2}{r} \sum_{n=0}^{\infty} (2n+1)(-iA_n) P_n(\cos\theta) \right] \exp[i(k_s r)] \\ &= \frac{p_o a}{2r} f_{\infty}(\theta, a) \exp[i(k_s r)] \end{aligned} \quad (3.5)$$

where the form factor is given by

$$f_{\infty}(\theta, a) = -\frac{2}{k_s a} \sum_{n=0}^{\infty} (2n+1)iA_n P_n(\cos\theta) \quad (3.6)$$

and

$$iA_n = \sin\eta_n \exp[-i\eta_n] = \frac{\tan\eta_n}{1 + i \tan\eta_n} \quad (3.7)$$

The form factor depends on the dimensionless parameter $k_s a$, which is the ratio of the particle circumference to the wavelength of the incident wave. This dependence can be divided into three regions: the Rayleigh or long-wavelength region ($k_s a \ll 1$); the Mie or diffraction region ($k_s a \approx 1$); and the geometric or short wavelength region ($k_s a \gg 1$). The form factor depends on the properties of the scatterer through the $\tan\eta_n$. In addition to the elastic case, special cases considered in this chapter are the rigid movable case and the rigid

immovable case.

For the rigid movable limit, $\mu' \rightarrow \infty$, so $x', s' \rightarrow 0$, and using the asymptotic forms of j_n and n_n for small argument, we have [Faran, 1951; Hay and Mercer, 1985]

$$\tan \Phi_n \rightarrow 0, \quad n \neq 0; \quad \tan \Phi_1 \rightarrow \frac{\rho_o}{\rho_o'} \quad (3.8)$$

Using Eq. (3.8) in Eq. (3.2), we get

$$\tan \eta_n = -\frac{j_n'(x)}{n_n'(x)}, \quad n \neq 1; \quad \tan \eta_1 = \frac{x(\rho_o/\rho_o')j_1'(x) - j_1(x)}{-x(\rho_o/\rho_o')n_1'(x) + n_1(x)} \quad (3.9)$$

For the rigid immovable case $\mu' \rightarrow \infty$, and $\rho_o'/\rho_o \rightarrow \infty$, $\tan \Phi_1$ also vanishes (Eq. 3.8), and we have

$$\tan \eta_n = -\frac{j_n'(x)}{n_n'(x)} \quad (3.10)$$

for all n .

3.2 Numerical results

We evaluated the form factor at intervals of 0.01 in x from the phase shifts η_n using the above expressions. The computations were made on a VAX 11/785 computer in double precision using the International Mathematics and Statistics

Library to evaluate the Bessel functions. The range of k , as chosen for the computations was 0.01 to 30.0. This spans most of the operating frequency range of interest (0.1 to 10.0 MHz) for the sand size range ($30 \mu\text{m}$ to 2 mm radius).

The values of the form factor for four cases at $\theta = 120^\circ$ for quartz in water at 15°C are presented in Fig. 5. These are the elastic case (Fig. 5a), the rigid movable case (Fig. 5b), the rigid immovable case (Fig. 5c), and the so-called "high-pass" model (Fig. 5d). The latter is discussed in a later section. The physical properties used for quartz and water are given in Table 2.

From Fig. 5 we note that the form factor in the Rayleigh region ($x \ll 1$) in the first three cases are similar. In the Mie region ($0.2 < x < 3$), the shapes of $|f_\infty|$ in both the elastic case and the rigid movable case are nearly the same. However, values in the rigid immovable case are larger. In the geometric region $|f_\infty|$ in the elastic case exhibits irregular variations. These variations are associated with resonances, and have been discussed elsewhere [Hay and Mercer, 1985, Flax et al, 1981]. However $|f_\infty|$ in both the rigid movable and the rigid immovable case oscillates regularly as x increases, and $|f_\infty| \rightarrow 1$ at very large x . Since $\mu \rightarrow \infty$ in these cases, resonance excitation does not occur.

The first and the second resonances are located at $x = 5.7$ and $x = 7.1$ [Hay and Mercer, 1985, Table II]. From Figs. 5a and 5b we note that the behavior of $|f_\infty|$ for $x < 5$ in both the elastic and rigid movable cases is nearly the same. This means the scatterer is in rigid body motion for values of x below about five, and the elastic vibrations are confined to the geometric range [Hickling, 1962].

Table 2. Elastic properties of the sediments used in calculation*

Quartz			
Density	ρ_0	$2.65 \times 10^3 \text{ kg m}^{-3}$	
Compressional wave speed	c_p	5100 m s^{-1}	
Shear wave speed	c_s	3200 m s^{-1}	
Granitic Gneiss			
Density	ρ_0	$2.84 \times 10^3 \text{ kg m}^{-3}$	
Compressional wave speed	c_p	4011 m s^{-1}	
Shear wave speed	c_s	2020 m s^{-1}	
Granite			
Density	ρ_0	$2.653 \times 10^3 \text{ kg m}^{-3}$	
Compressional wave speed	c_p	4192 m s^{-1}	
Shear wave speed	c_s	2791 m s^{-1}	
Sandstone Quartzite			
Density	ρ_0	$2.655 \times 10^3 \text{ kg m}^{-3}$	
Compressional wave speed	c_p	5191 m s^{-1}	
Shear wave speed	c_s	3498 m s^{-1}	
Water**			
Density	ρ_0	$0.998 \times 10^3 \text{ kg m}^{-3}$	
Speed of sound	c	1466 m s^{-1}	

* All the data come from *Handbook of Physical Constants* [Clarke, 1966], and we use the average value if there are several values available for the same material.

** The sound speed in the water is calculated using the formula given by Clay and Medwin [1977, p. 88]. T is the temperature, which is chosen as $T = 15^\circ \text{C}$ here.

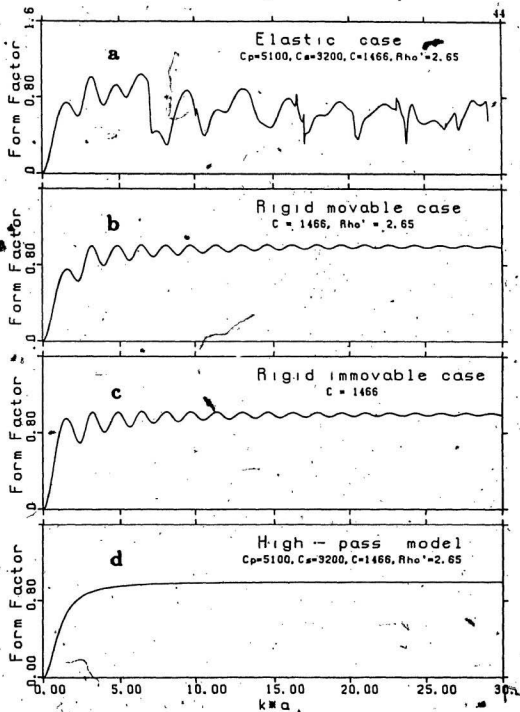


Figure 5 Calculated values of $|f_\infty|$ at scattering angle $\theta = 120^\circ$ for four theoretical models. (a) elastic case; (b) rigid movable case; (c) rigid immovable case; (d) High-pass model.

3.3 Analytic expressions for $|f_{\infty}|$

In general, sand grains are irregularly shaped and inhomogeneous in composition. Under these conditions resonance excitation is unlikely, and f_{∞} for the rigid movable case should be more suitable. If in addition the size distribution is sufficiently broad, the oscillatory behavior of f_{∞} would be averaged out. We therefore seek a smooth analytic function which approximates the average form of f_{∞} . This kind of concept was introduced by Johnson [1977] for fluid spheres in the backscattering case. In this section we present the equivalent result for solid spheres and arbitrary scattering angle.

In the Rayleigh region ($x, x', s' \ll 1$), the form factor in Eq. (3.6) reduces to the well known result [Rayleigh 1945, p.283]

$$f_{\infty}(\theta, a) \approx \frac{2}{3}(k_c a)^2 (\gamma_{\kappa} + \gamma_{\rho} \cos \theta) \quad (k_c a \ll 1) \quad (3.11)$$

with

$$\gamma_{\kappa} = \frac{\kappa' - \kappa}{\kappa} \quad (3.12)$$

and

$$\gamma_{\rho} = \frac{3(\rho'_0 - \rho_0)}{2\rho'_0 + \rho_0} \quad (3.13)$$

where κ is the adiabatic compressibility of the fluid, and $\kappa'_0 = 1/(\lambda' + 2\mu'/3)$ is the bulk compressibility of the solid. For quartzlike materials in the water, using

the parameter values in Table 2, we have $\gamma_x \sim -0.9$ and $\gamma_p \sim 0.8$.

In the geometric region ($x, x', s' \rightarrow \infty$), we consider the rigid movable case. Substituting Eq. (3.9) in Eq. (3.6), we have

$$f_{\infty}(\theta, a) = \frac{6i}{z} \frac{h_1(x)j_1'(x) - j_1(x)h_1'(x)}{x(\rho_s'/\rho_s)h_1'(x)h_1''(x) - h_1(x)h_1'(x)} \frac{1}{\cos\theta} + \frac{2i}{z} \sum_{n=0}^{\infty} (2n+1)P_n(\cos\theta) \frac{j_n'(x)}{h_n(x)} \quad (3.14)$$

where $h_n(x) = j_n(x) + in_n(x)$.

Following Hickling and Wang [1965], the above equation can be written as

$$f_{\infty}(\theta) = G(\theta) + \hat{f}(\theta) \quad (3.15)$$

where $G(\theta)$ and $\hat{f}(\theta)$ represent the corresponding terms in Eq. (3.14), and $\hat{f}(\theta)$ is the form factor for the rigid immovable case. In the limit $k_c a \rightarrow \infty$, $\hat{f}(\theta)$ is given by [Morse and Feshbach, 1953, p. 1554]

$$\hat{f}(\theta) \approx \exp \left[-2iz \sin \left(\frac{\theta}{2} \right) \right] + iz \left[\left(\frac{1+\cos\theta}{x \sin\theta} \right) J_1(x \sin\theta) \right] \quad (z \rightarrow \infty) \quad (3.16)$$

The first term on the right hand side in the above equation is an isotropically scattered wave, the second term is the shadow-forming wave. Comparing this term with the transducer directivity (Eq. 2.21), we see that it is sharply peaked in the forward direction for large $k_c a$. Since we are interested in the bistatic and monostatic systems for which θ is large, and since $J_1(z) \sim 1/\sqrt{z}$ for large z , we have

$$f(\theta) \approx \exp[-2iz \sin(\frac{\theta}{2})] \quad (z \rightarrow \infty) \quad (3.17)$$

Using the asymptotic forms of the Bessel functions for large argument, $G(\theta)$ can be shown to reduce to

$$G(\theta) \approx -\frac{6\rho_s}{\rho_s z^2} e^{-2iz \cos \theta} \quad (z \rightarrow \infty) \quad (3.18)$$

This result is similar to that given by Hickling and Wang [1965], except for a difference in the sign of $G(\theta)$, and the additional factor of $\cos \theta$. Comparing Eqs. (3.16) and (3.17), we see that $G(\theta)$, which results from the mobility of a scatterer of finite mass, is unimportant at large z , and so for $\theta \neq 0$

$$|f_\infty| \rightarrow 1 \quad (z \rightarrow \infty) \quad (3.19)$$

It is now possible to construct an expression for $|f_\infty|$ which possesses the appropriate asymptotic behavior in both the Rayleigh and the geometric regions. Following Johnson [1977] we write

$$|f_\infty(\theta, a)| \approx \frac{K_f z^2}{1 + K_f z^2} \quad (0 \leq z < \infty, \theta \neq 0) \quad (3.20)$$

where

$$K_f = \frac{2}{3} |(\gamma_k + \gamma_p \cos \theta)| \quad (3.21)$$

For quartz in water and a scattering angle of 120° , using the estimates of γ_k and γ_p calculated previously, we get $K_f = 0.9$.

Eq. (3.21) is plotted in Fig. 5d for $\theta = 120^\circ$ and $K_f = 0.884$. Since its shape is similar to the gain of a high-pass filter, it is called the "high-pass" model. Comparing Fig. 5d with Figs. 5a, 5b and 5c, we note that the form factor in the high-pass model approaches that in the rigid movable case with the oscillations averaged out.

3.4 The dependence of $|f_\infty|$ on scattering angle

The form factor given in (Eq. 3.6) is a function of scattering angle. In Chapter 2 we stated that this dependence would be discussed in two contexts. One had to do with the integral of scattered pressure over the detected volume (Eq. 2.11), the other with multiple scattering and the forward scattered waves. We discuss the latter case first.

The form factor in the forward direction for a quartz sphere in water, calculated using the elastic model, is plotted in Fig. 6. We note that on average $|f_\infty|$ increases linearly with z . This is readily shown in the rigid case, Eq. (3.16), which reduces to

$$|f_\infty(0)| \rightarrow z \quad (z \rightarrow \infty) \quad (3.23)$$

The amplitude of the forward scattered wave therefore becomes very large as z increases, and it is for this reason that it was given separate consideration in the discussion of multiple scattering in Chapter 2.

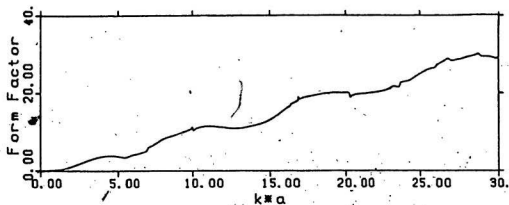


Figure 6. The form factor in the forward direction for quartz in water.

In Chapter 2 we also assumed that $|f_{\infty}(\theta)|^2 = |f_{\infty}(\theta_s)|^2$ throughout the detected volume for narrow beam patterns. In the following discussion we test the validity of this assumption. Consider a typical system in which $-\theta_s = 120^\circ$ and $\beta_s = 1^\circ$. In this case $\theta_{\max} = 122^\circ$ and $\theta_{\min} = 118^\circ$. Let

$$\text{DEL1} = |f_{\infty}(120^\circ)| - |f_{\infty}(118^\circ)| \quad (3.24)$$

and

$$\text{DEL2} = |f_{\infty}(120^\circ)| - |f_{\infty}(122^\circ)| \quad (3.25)$$

The numerical results for Eqs. (3.24) and (3.25) in the elastic case are shown in Fig. 7. From this diagram and Fig. 5 we note that most of the difference values are much less than $|f_{\infty}|$. As a result, $|f_{\infty}(\theta_j, a_j)|^2$ in Eq. (2.8) could be a

expressed as a linear function of the Cartesian coordinates X and Z on which θ_j depends. We also note from Fig. 7, however, that $\text{DEL1} \sim -\text{DEL2}$. Therefore, since the detected volume is symmetric in X , and for narrow beam systems is nearly symmetric in Z , the variations in $|f_\infty|^2$ tend to cancel.

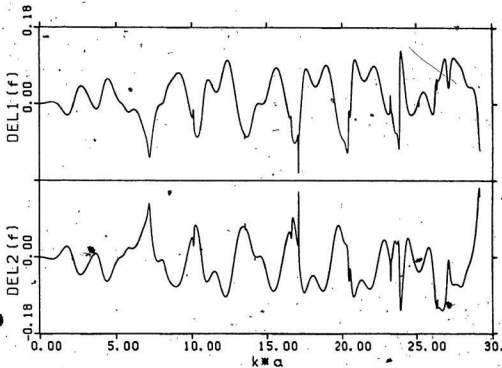


Figure 7. The difference of $|f_\infty|$ in the narrow beam pattern.

CHAPTER 4 THE ATTENUATION COEFFICIENT

The theoretical computation of the attenuation coefficient due to scattering loss α_s is made in this chapter for the elastic sphere, and for the rigid-movable sphere and the rigid-immovable sphere as well. A smooth analytic function which approximates the average α_s is introduced in Section 4.2.

In addition to absorption in the fluid, the attenuation of sound waves in suspensions arises from the energy scattered to infinity and the energy absorbed within and in the neighborhood of the scatterer. The total linear attenuation coefficient can be expressed in the form

$$\alpha = \alpha_a + \alpha_p = \alpha_a + \alpha_t + \alpha_v + \alpha_s, \quad (4.1)$$

where α_a is the attenuation coefficient in the ambient fluid, and the additional attenuation α_p due to the presence of the scatterers is the sum of: α_t , the thermal attenuation; α_v , the viscous absorption; and α_s , the scattering loss.

For aqueous suspensions of mineral grains, Hay and Burling [1982] have shown that thermal attenuation is small. Hay and Mercer [1985] have shown that viscous attenuation can be ignored outside the Rayleigh range. Therefore we have

$$\alpha \approx \alpha_a + \alpha_s. \quad (4.2)$$

In dilute suspensions, for which the effect of the individual particles is additive, the attenuation due to scattering can be written as [Allegra and Hawley, 1972]

$$\alpha_s = \frac{3\epsilon}{2k_c^2 a^3} \sum_{n=0}^{\infty} (2n+1) |A_n|^2 \quad (4.3)$$

where ϵ is the volume concentration of scatterers, which is defined as

$$\epsilon = \frac{M}{\rho_s} \quad (4.4)$$

where M is the mass concentration of suspended particles.

Because we have ignored viscosity and heat conduction, $\tan \eta_n$ is real, so that using Eq. (3.7), Eq. (4.3) can be written as

$$\alpha_s = \frac{3\epsilon}{2k_c^2 a^3} \sum_{n=0}^{\infty} (2n+1) \frac{\tan^2 \eta_n}{1 + \tan^2 \eta_n} \quad (4.5)$$

The form factor in Eq. (3.6) for $\theta = 0$ in this case can be written as

$$f_{\infty}(0) = -\frac{2}{k_c a} \sum_{n=0}^{\infty} (2n+1) \frac{\tan \eta_n (1 - i \tan \eta_n)}{1 + \tan^2 \eta_n} \quad (4.6)$$

Therefore α_s in Eq. (4.5) becomes

$$\frac{a \alpha_s}{\epsilon} = \frac{3}{4} \frac{\text{Im}[f_{\infty}(0)]}{x} \quad (4.7a)$$

or

$$\frac{\rho_s \alpha_s}{k_c M} = \frac{3}{4} \frac{\text{Im}[f_{\infty}(0)]}{x^2} \quad (4.7b)$$

The difference between Eq. (4.7a) and Eq. (4.7b) is that the left-hand side of Eq. (4.7a) depends on concentration and the radius of the particle, whereas the left-hand side of Eq. (4.7b) depends on concentration and frequency. The latter form is useful when we consider the effect of size distributions.

4.1 Numerical results

The attenuation coefficient α_r for quartz in water calculated at intervals of 0.01 in x is plotted in Fig. 8 (normalized according to Eq. 4.7a) and Fig. 9 (normalized according to Eq. 4.7b) for the elastic (Figs. 8a and 9a), rigid movable case (Figs. 8b and 9b), and rigid immovable case (Figs. 8c and 9c). Also shown is the high-pass model (Figs. 8d and 9d), which is discussed later.

From these Figures we note that in the Rayleigh region α_r/ϵ for all four cases are equivalent. In the Mie region ($0.2 < x < 3$), α_r/ϵ in both the elastic and the rigid movable cases are nearly the same, but in the rigid immovable case the attenuation is larger. In the geometric region all models are similar, except for the oscillations in the elastic case, which are associated with resonances [Hay and Mercer, 1985]. Comparing Fig. 5a with Fig. 8a, the attenuation coefficient is a much smoother function of x than is the form factor.

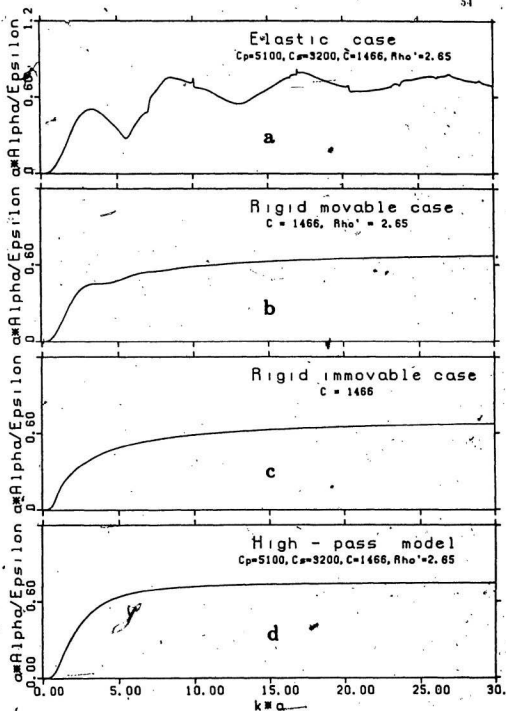


Figure 8 Calculated values of α/ϵ for four theoretical models.
 (a) elastic case; (b) rigid movable case; (c) rigid immovable case; (d) high-pass model.

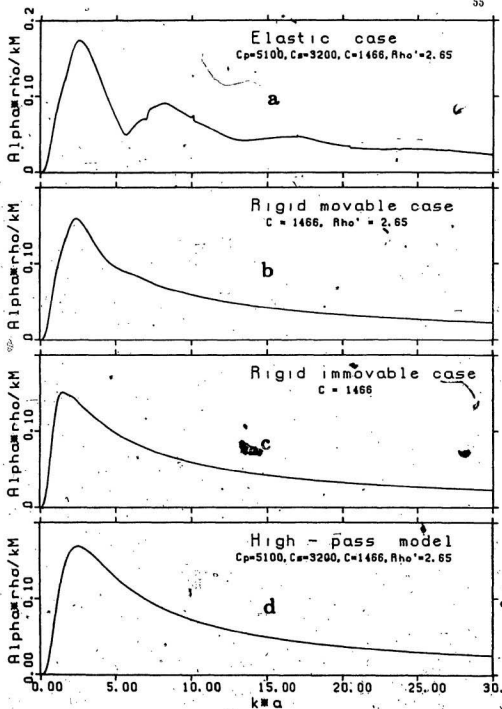


Figure 9 Calculated values of $\rho_0' \alpha / k_c M$ for four theoretical models.
 (a) elastic case; (b) rigid movable case; (c) rigid immovable case; (d) high-pass model.

4.2 Analytic expressions for α_s

Referring to Hay and Burling [1982], in the Rayleigh range ($x, z, d \ll 1$), $|\eta_s| \ll 1$, so that the coefficients $\tan \eta_s$ rapidly become negligible as n increases. We therefore consider only the first two coefficients $\tan \eta_s$ and $\tan \eta_1$. The expression for α_s in this case is given by [Allegra and Hawley, 1972]

$$\frac{a \alpha_s}{\epsilon} \approx \frac{z^4}{6} \left(\gamma_s^2 + \frac{\gamma_p^2}{3} \right) \quad (k_s a \ll 1) \quad (4.8)$$

Now consider the geometric region ($x \rightarrow \infty$) and the rigid immovable case. From Eq. (3.16) we have

$$\text{Im } \hat{f}(0) \approx z \quad (4.9)$$

Substituting the above equation into Eq. (4.7), we finally get

$$\frac{a \alpha_s}{\epsilon} \rightarrow \frac{3}{4} \quad (z \rightarrow \infty) \quad (4.10)$$

This result has already been used in Chapter 2 (Eq. 2.36).

As with the high pass model for the form factor (Eq. 3.20), we can construct a similar simple expression for the attenuation coefficient. Based on Eqs. (4.8) and (4.10), we write the attenuation coefficient as follows

$$\frac{a \alpha_s}{\epsilon} = \frac{K_o z^4}{1 + (4/3) K_o z^4} \quad (4.11)$$

where

$$K_o = \frac{1}{6} \left[\eta_z^2 + \frac{\gamma_p^2}{3} \right] \quad (4.12)$$

For quartz in water at $T = 15^\circ \text{C}$, $K_o \approx 0.2$.

Comparing this expression with the results for the other cases, we find that it provides a reasonable fit for very small z and very large z , but not in the Mie region. We therefore introduce the following formula

$$\frac{\rho_o \alpha_r}{\epsilon} = \frac{K_o z^4}{1 + (4/3)K_o z^4 + z^2} \quad (4.13a)$$

$$\frac{\rho_o \alpha_r}{k_r M} = \frac{K_o z^3}{1 + (4/3)K_o z^4 + z^2} \quad (4.13b)$$

The effect of the z^2 terms is to reduce the magnitude of α_r near $z \sim 1$. Again we call it a "high-pass" model.

From Figs. 8 and 9 it is seen that the high-pass model provides a better fit to the elastic and rigid movable cases than the rigid immovable model in the region $1 < k_r a < 3$.

CHAPTER 5 COMPARISON WITH DATA

The theoretical results for attenuation coefficient and mean square scattered pressure presented in the previous chapters are compared with data in this chapter. The multiple scattering problem is also discussed briefly. The effects of different size distributions on attenuation coefficient and scattered intensity are included.

5.1 The data

Jansen [1977] used a bistatic system operating at 8 MHz to measure the mean square signal voltage $\overline{V^2}$, which is proportional to the scattered intensity, from suspended sand grains. The system parameters are summarized in Table 3. Four size fractions were tested: 45 to 62.5 μm ; 105 to 125 μm ; 175 to 210 μm and 250 to 300 μm radius. The sediment concentrations were in the range $0.1 < M < 30 \text{ kg/m}^3$. In 1979 Jansen repeated his experiments using the same size fractions. The second set of results were not published, but are used here. In both experiments the sand grains were not distributed throughout the test chamber, but were instead allowed to free fall through a 3 cm wide rectangular perspex tube coaxial with the detected volume.

Jansen's measurements of mean square signal voltage as a function of sand concentration are reproduced in Fig. 10. It can be seen that the signal depends linearly on sediment concentration for $M < 1 \text{ kg/m}^3$. In the range $M > 1 \text{ kg/m}^3$, the effects of attenuation become important. The mean square voltage exhibits significant variation with grain size.

Table 3. The parameters of the acoustic systems.

Data sources: (a1) Jansen, [1977]; (a2) Jansen, [1979]; (b1) 1-D and (b2) 2-D from Schaafsma and der Kinderen, [1985] and (c) Clarke et al., [1984]. NS represents "not specified".

Source of Data	r_o (cm)	β_o	θ_o	Frequency (MHz)	T (°C)	k_c $10^4 \text{ (m}^{-1}\text{)}$
(a1)	15	1°	120°	8.0	NS	3.43
(a2)	15	1°	120°	8.0	-15	3.43
(b1)	15	2°	120°	4.5	15	1.95
(b2)	15, 7.5	2°	120°	4.5	15	1.95
(c)	NS	NS	180°	3.0	20	1.27

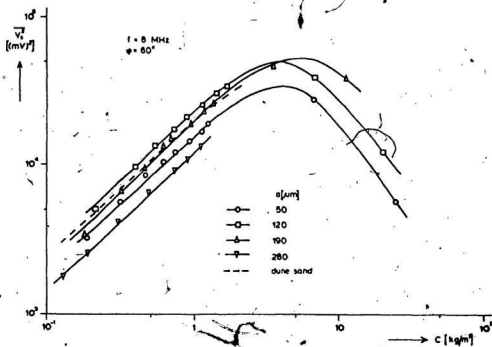


Figure 10. The mean square scattered signal as a function of sand concentration for various grain radii (from Japsen [1977]).

Schaafsma and der Kinderen [1985] used two types of bistatic system operating at 4.5 MHz. One system is called one-dimensional (1-D), the other two-dimensional (2-D). Both systems consist of a transmitting transducer and two receiving transducers. The difference between them is that in the one-dimensional system one of the receiving transducers is used to detect the transmitted signal, the other to detect the scattered signal. In the two-dimensional system, however, both receiving transducers are used to detect scattered signals, but at different values of r_s . This difference is not important here, but the distinction is retained to differentiate between the data sets. The other system parameters are summarized in Table 3. Schaafsma and der Kinderen used natural sand distributions in the size range of 38 to 60 μm ; 55 to 108 μm ; and 65 to 125 μm radius in the one-dimensional system, and 34 to 70 μm ; 53 to 120 μm ; and 75 to 160 μm radius in the two-dimensional system. These ranges are half the D_{16} and D_{84} values, where D_{16} and D_{84} mean that 16% and 84% of the grains are smaller than the diameter D . The sediment concentration range was $0 < M < 5 \text{ kg/m}^3$. Unlike Jansen's experiments, sand grains were distributed throughout the test chamber.

The signals from the two-dimensional system are reproduced in Fig. 11, where $r_s = 7.5 \text{ cm}$ for receiver 1 and $r_s = 15 \text{ cm}$ for receiver 2. Note that both scales are linear, unlike Fig. 10 in which both are logarithmic. From Fig. 11 it can be seen that the linear dependence of the mean-square voltage on M holds for $M \leq 0.5 \text{ kg/m}^3$. For larger values of M the effects of attenuation are important. It is also seen that at lower concentrations, the signals do not depend significantly on grain size. Note that Schaafsma and der Kinderen used a much

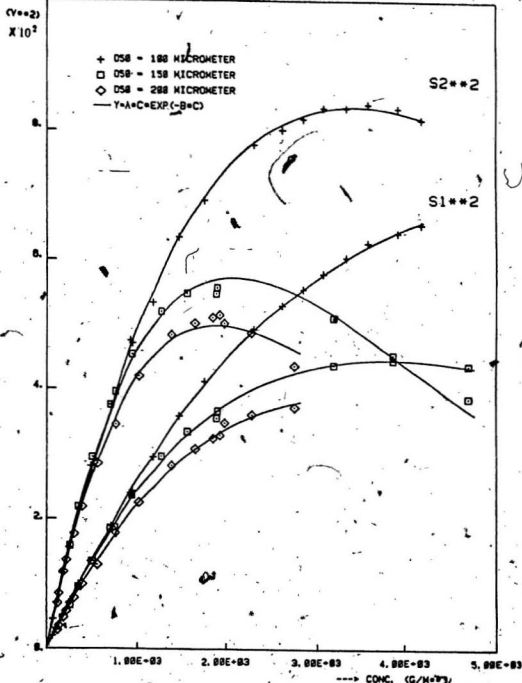


Figure 11. The mean square scattered signal from the 2-dimensional system. S_1^2 is the output signal from receiver 1 and S_2^2 is the output signal from receiver 2 (from Schaafsma and der Kin [1985]).

smaller range of grain sizes than Jansen. For larger concentrations, however, the mean square voltage exhibits significant variation with grain size.

Clarke et al. [1984] have reported the measurements of scattered intensity for three size fractions of sand in a monostatic system operating at 3 MHz. The other system parameters are summarized in Table 3. While this thesis relates mainly to bistatic systems, the discussions in Chapter 2 also hold for the monostatic case, and these data can therefore be included. Clarke et al. used size fractions of 37 to 55 μm , 70 to 90 μm and 153 to 227 μm radius. Unlike Jansen's and Schaafsma and der Kindersen's experiments in which the size fractions were simply separated by sieving, the size distributions in this case were determined by measuring the major and minor axes of individual grains using an optical microscope. The values given here are the minor radii at which the probability densities of the size distribution are half the peak values. The concentration range was $0 < M < 0.1 \text{ kg/m}^3$.

5.2 Measured and theoretical attenuation coefficients

5.2.1 Estimating α_s from the measurements

From Eq. (2.70), we have

$$\log_{10} [\hat{p}_s^2 / M] = \text{constant} - 4 \bar{\alpha}_s r_s \log_{10} \epsilon \quad (5.1)$$

Referring to Eq. (4.7), $\bar{\alpha}_s$ is linearly proportional to M and it can therefore be seen from Eq. (5.1) that $\log_{10} [\hat{p}_s^2 / M]$ is a linear function of M . It should be mentioned here that this linear dependence will not hold when multiple scattering

becomes important.

The measured values of $\log_{10}[\dot{p}_s^2/M]$ as a function of concentration for Jansen's data are shown in Fig. 12. The plotted points were calculated from the measured values as determined graphically from Fig. 10. The solid lines represent the visual best fit. The linear dependence of $\log_{10}[\dot{p}_s^2/M]$ on M is satisfied for $0.5 < M < 10 \text{ kg/m}^3$. Attenuation is not important for concentrations less than 0.5 kg/m^3 . The data also indicate that for M significantly greater than 10 kg/m^3 , the attenuation coefficient is no longer linear (Fig. 12b). The discussion will return to this point. The measured values of $\log_{10}[\dot{p}_s^2/M]$ as a function of concentration from Schaafsma and der Kinderen's results are shown in Fig. 13. Again the solid lines represent the visual best fit to the data. It is seen that the linear dependence of $\log_{10}[\dot{p}_s^2/M]$ on M is nearly perfect in this concentration range ($M \leq 5 \text{ kg/m}^3$).

5.2.2 Comparison assuming uniform particle size

Values of $\bar{\alpha}\bar{\alpha}_s/\epsilon$ were computed from the slopes of the lines in Figs. 12 and 13, where $\bar{\alpha}$ is mean radius in each size fraction, taken to be the average of the size range representing each fraction. For comparison, theoretical estimates were obtained from the calculated values in Fig. 8, assuming uniform size equal to the mean radius. The calculated and measured values of $\bar{\alpha}\bar{\alpha}_s/\epsilon$ are given in Table 4. The measured value of $\bar{\alpha}\bar{\alpha}_s/\epsilon$ for $\sigma = 280 \mu\text{m}$ in Jansen's [1977] data has been dropped, since the data points are all at low concentrations and it is therefore difficult to estimate the slope accurately (Fig. 12a).

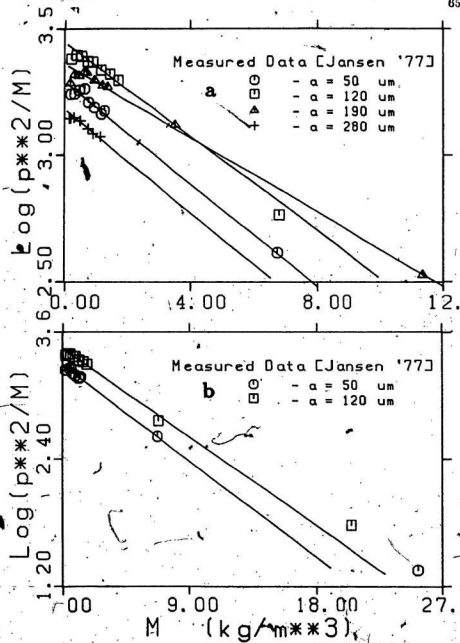


Figure 12. $\log_{10}(p^2/M)$ vs M for data given by Jansen [1977].
 (a) at low concentrations; (b) over the entire range of concentration
 in the experiments for $\bar{\alpha} = 50$ and $120 \mu\text{m}$ (see also Fig. 10).

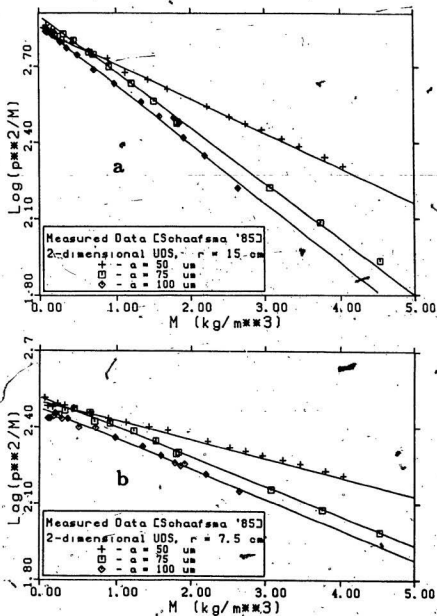


Figure 13. $\log_{10}[\tilde{p}^2/M]$ vs M for data given by Schaafsma and der Kinderen [1985]. (a) from S_2^2 ; (b) from S_1^2 (see also Fig. 11).

The measured and theoretical values are compared in Fig. 14 (Jansen's data) and Fig. 15 (Schaafsma and der Kinderen's data). Agreement between theory and experiment is generally reasonable. For comparison of the different theoretical cases, we consider mainly Fig. 15, since attenuation coefficients estimated from Schaafsma and der Kinderen's data are probably more reliable, given the higher density of measured points (see Figs. 12 and 13). Although the size range is limited, it can be seen that the theoretical curves for the elastic, rigid-movable and high pass cases fit the data quite well. The theoretical estimates in the rigid-immovable case, however, are high.

Table 4. Calculated and measured values of $\bar{\alpha} \bar{\sigma}_s / \epsilon$ assuming uniform particle size. Data sources: (a) Jansen, [1977] and [1979]; (b1) 1-D and (b2) 2-D from Schaafsma and der Kinderen, [1985]. "Movable" and "Immovable" refer to the rigid movable case and rigid immovable case, respectively.

Sand			$\bar{\alpha} \bar{\sigma}_s / \epsilon$				$\bar{\alpha} \bar{\sigma}_s / \epsilon$
Source	$\bar{\sigma}$ (μm)	$k_s \bar{\sigma}$	Elastic	Movable	Immovable	High-pass	Measured
(a)	54	1.84	0.262	0.263	0.272	0.289	0.256, 0.178
	115	3.96	0.473	0.455	0.444	0.583	0.566, 0.531
	193	6.60	0.448	0.539	0.536	0.683	0.706, 0.522
	275	9.43	0.731	0.582	0.582	0.716	0.655
(b1)	50	0.96	0.066	0.071	0.110	0.072	0.067
	80	1.54	0.182	0.191	0.233	0.214	0.168
	100	1.93	0.288	0.286	0.284	0.300	0.235
(b2)	50	0.96	0.066	0.071	0.110	0.072	0.075
	75	1.45	0.162	0.171	0.219	0.192	0.176
	100	1.93	0.288	0.286	0.284	0.310	0.242

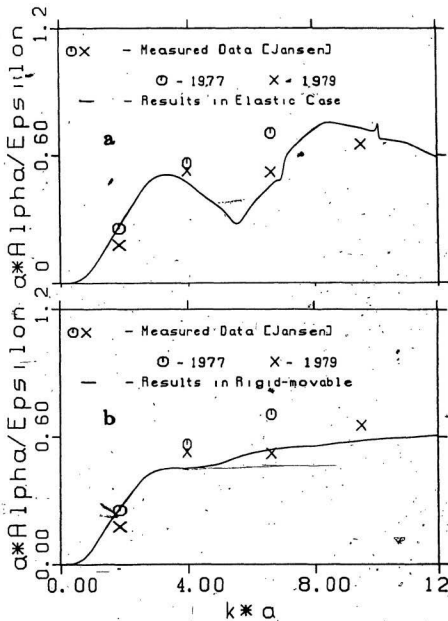


Figure 14a and b. Comparison of measured and computed values of $\frac{\alpha \cdot \text{Alpha}}{\epsilon}$ using Jansen's data. The theoretical curves are for: (a) the elastic case; (b) the rigid movable case.

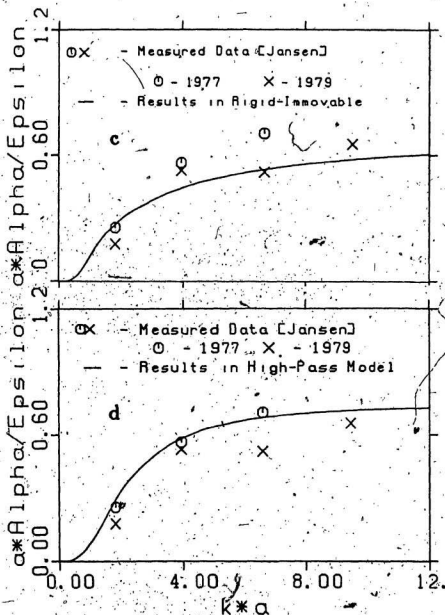


Figure 14c and d. Comparison of measured and computed values of $\bar{\sigma}_0/\epsilon$ using Jansen's data. The theoretical curves are for: (c) the rigid immovable case; (d) high-pass model.

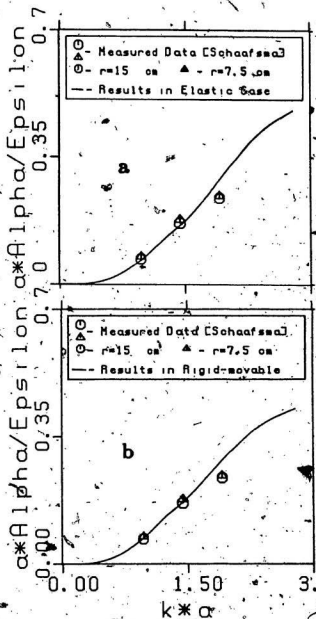


Figure 15a and b. Comparison of measured and computed values of $\frac{\alpha \cdot \text{Alpha}}{\epsilon}$ using Schaafsma and der Kinderen's data. The theoretical curves are for: (a) the elastic case; (b) the rigid movable case.

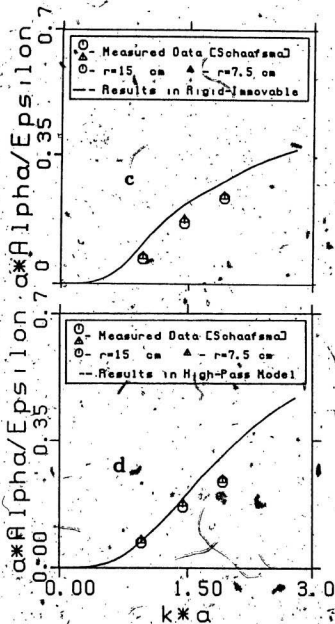


Figure 15c and d. Comparison of measured and computed values of $\alpha \cdot \text{Alpha} / \text{Epsilon}$ using Schaafsma and der Kinderen's data. The theoretical curves are for: (c) the rigid immovable case; (d) high-pass model.

The calculated and measured attenuation coefficients are plotted in Fig. 16 for the four models. The abscissa is the measured value, the ordinate the theoretical estimate. R_{xy} is the cross-correlation coefficient [e.g. Beyer 1981, p.510]. From Fig. 16 it can be seen that the linear relationship between the theoretical estimates and the measured values of attenuation coefficient in all four cases is very good. Some reduction in the degree of scatter is to be expected if size distributions of finite width are used in the computations, since this would effectively cause additional smoothing of the theoretical attenuation coefficients. This is considered later.

5.2.3 Multiple scattering

We now return to the observation that the attenuation coefficient at sufficiently high concentrations becomes a nonlinear function of M (Fig. 12b). This was observed only at concentrations well above 10 kg/m^3 , and measurements were made at such concentrations only for two sand sizes: $54 \mu\text{m}$ and $115 \mu\text{m}$ mean radius, corresponding to values of x of 1.84 and 3.96 respectively. Using Eq. (3.6) the form factor $|f_\infty|$ has been calculated for three scattering angles: 0° , 120° and 180° . For $x = 1.84$, the values are 0.77, 0.71 and 0.68 respectively. These are nearly the same, and the isotropic scattering model is assumed in this case. For $x = 3.96$, the values are 3.62, 0.73 and 1.26 respectively. It is clear that forward scattering dominates at this value of x . The tendency for the rate of increase of $\bar{\sigma}_t$ with increasing M to decrease at high concentrations is well known, and is the result of multiple scattering [e.g. Urlick, 1948; Ma et al., 1984].

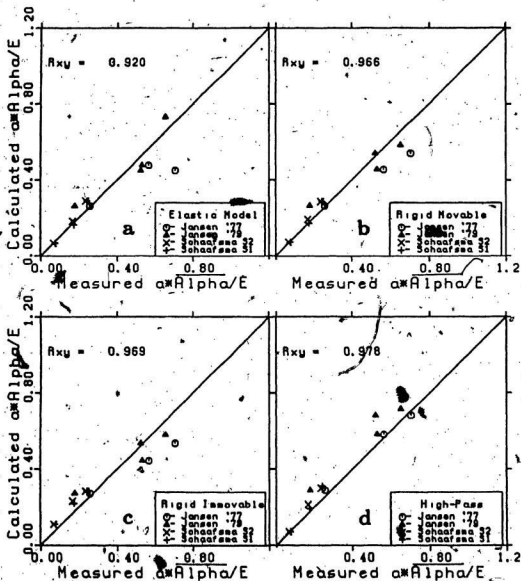


Figure 16. Calculated and measured values of $\alpha\Delta/c$ for uniform particle size. (a) elastic case; (b) rigid movable case; (c) rigid immovable case; (d) high-pass model. In these and subsequent figures the solid line represents perfect agreement between theory and experiment, not the best fit straight line.

For $x = 1.84$, the total multiple scattered pressure can be estimated from Eq. (2.74). Since the sand grains in Jansen's experiments were confined in a 3 cm wide rectangular tube, the ranges of $\delta + \rho$ and Φ in this case are the same as in Eqs. (2.75) and (2.76), but the range of ρ is limited to $r^* \leq \rho \leq r_{ij} + \lambda/4$, where r^* is the distance from the cylinder to the receiver (see Fig. 17). It can be seen that r^* changes with β . For simplicity, considering the narrow beam case, we assume r^* is constant, and equal to 2 cm in Jansen's experiments. The multiple scattered pressure then takes the form

$$\frac{P_{1j}}{p_{sj}} = \frac{3f_{\infty} M(r_s - r^*)}{2k_s a^2 \rho_s} \quad (5.2)$$

For $M = 25.5 \text{ kg/m}^3$, $\rho_s = 2.65 \times 10^3 \text{ kg/m}^3$, and $|f_{\infty}| = 0.7$, we get $|P_{1j}/p_{sj}| \approx 3.0$. For a single particle in the detected volume, the total scattered pressure at the receiving transducer is $p_{sj} + P_{1j}$. Ignoring phase differences between the scattered and rescattered waves, the total scattered pressure becomes

$$\left[1 + \left| \frac{P_{1j}}{p_{sj}} \right| \right] \bar{p}_s$$

which at this concentration is about $4.0 \bar{p}_s$, where \bar{p}_s is the mean scattered pressure without multiple scattering. From Fig. 12b, we find graphically that the actual scattered pressure at this concentration is $1.9 \bar{p}_s$. The approximate predicted correction is therefore within a factor of two of that observed.

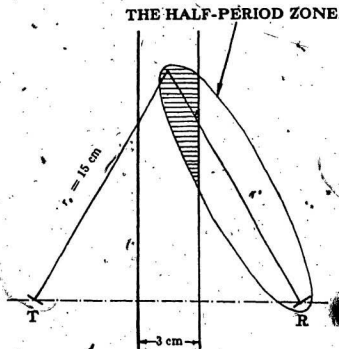


Figure 17. The geometry in Jansen's experiments. The 3 cm wide rectangular perspex tube through which the sand grains were allowed to fall is shown in the center of the sketch.

For $z = 3.96$, we consider forward multiple scattering only. In this case the multiple scattered pressure can be estimated using Eq. (2.88), but with r^* for the upper limit for δ . Working out the algebra, we get

$$\frac{P_{1j}}{p_{sj}} = \frac{af_{\infty}(0)N^{\frac{1}{3}}}{2} \ln \left[\frac{r_s - r^*}{f^*} r_s N^{\frac{1}{3}} \right] \quad (5.3)$$

where N is the number of particles per unit volume. For uniformly sized scatterers, $N = 3M/(4\pi\rho_s a^3)$:

For $M_s = 20.5 \text{ kg/m}^3$, $\rho_s = 2.65 \times 10^3 \text{ kg/m}^3$, and $|f_{\infty}(0)| = 3.62$, we get $|P_{1j}/p_{sj}| \approx 0.8$. Again, the scattered pressure at the receiving transducer due to a single particle is $p_{sj} + P_{1j}$, but in this case it is possible to include the effects of the phase difference between the incident scattered wave and the forward rescattered wave. From Eq. (3.16) we see that the phase difference between the forward scattered wave and the incident wave is $\pi/2$. The total scattered pressure is therefore given approximately by

$$\left[1 + \left| \frac{P_{1j}}{p_{sj}} \right|^2 \right]^{\frac{1}{2}} \hat{p}_s = \sqrt{1 + 0.8^2} \hat{p}_s = 1.3 \hat{p}_s$$

From Fig. 12b the actual scattered pressure at this concentration is seen to be $1.2\hat{p}_s$. The agreement between the predicted and actual total scattered pressures is very good.

Now consider the apparent absence of multiple scattering effects in Schaafsma and Kinderen's results (Fig. 13). Since the maximum values of z in Schaafsma and der Kinderen's experiments are less than 2.0, the isotropic

scattering assumption is made. The multiple scattered pressure can be estimated using Eq. (2.79), which is $|P_{1j}/p_{sj}| \approx (1.5 \sim 4.5)$ for $r_s = 15$ cm and $|P_{1j}/p_{sj}| \approx (0.8 \sim 2.2)$ for $r_s = 7.5$ cm at $M = 5$ kg/m³. Again ignoring phase differences due to scattering, the total scattered pressure is about $(2.5 \sim 5.5) \bar{p}_s$ for $r_s = 15$ cm and $(1.8 \sim 3.2) \bar{p}_s$ for $r_s = 7.5$ cm. The predicted values are obviously too large. The failure of the theory is apparently due to the effects of ignoring phase differences between the scattered and rescattered waves, the transducer directivity, and the scattered pressure from particles in the second Fresnel zone. All of these would tend to reduce the estimate of total scattered pressure. The angular dependence of the phase difference, and of the transducer directivity in the near field, however, are not easily included.

From the above discussion it can be seen that the nonlinear dependence of the attenuation coefficient on M at high concentrations could be due to multiple scattering, and the approximate correction for cases in which forward scattering dominates ($z \gg 1$) is in reasonable agreement with the data. At smaller values of z consistency with experiment is possible only if the scatterers are restricted to the transducer far field, and even then the predicted effects are too large. A more complete approach is needed in this case.

6.2.4 Size distributions

We have now considered the effects of size distributions on attenuation and scattering. In this section we will compare measured values and theoretical estimates obtained by considering the effects of two simulated size distributions: the Gaussian and the Rayleigh distributions.

The Gaussian distribution is given by

$$n(a) = \frac{1}{\sqrt{2\pi}\sigma} \exp\left[-\frac{(a-\bar{a})^2}{2\sigma^2}\right] \quad (\sigma > 0) \quad (5.4)$$

where \bar{a} and σ are the mean value and the standard deviation, respectively. Let

a_{16} , a_{50} and a_{84} represent the radii at which $(1/N) \int n(a) da$ is equal to 0.16, 0.50 and 0.84, respectively (see Fig. 18). We have

$$\bar{a} = a_{50} \quad (5.5a)$$

$$\sigma = 0.51 \left(a_{84} - \frac{a_{16} + a_{84}}{2} \right) \quad (5.5b)$$

The Gaussian distribution in $k_e a$ -space can be expressed by

$$n(x) = \frac{n(a)}{k_e} = \frac{1}{\sqrt{2\pi}q} \exp\left[-\frac{(x-\bar{x})^2}{2q^2}\right] \quad (q > 0) \quad (5.6)$$

where $x = k_e a$, $\bar{x} = k_e \bar{a}$ and $q = k_e \sigma$.

The expression for A^2 in Eq. (2.15) takes the form

$$k_e^2 A^2 = \int_0^\infty \frac{x^2 |f_\infty|^2}{\sqrt{2\pi}q} \exp\left[-\frac{(x-\bar{x})^2}{2q^2}\right] dx \quad (5.7)$$

which will be used later, and the attenuation coefficient $\bar{\alpha}_s$ (Eq. 4.7) takes the form

$$\frac{\rho_s \bar{\alpha}_s}{k_s M} = \int_0^{\infty} \frac{3 \text{Im}[f_{\infty}(\theta)]}{4x^2} \frac{1}{\sqrt{2\pi q}} \exp\left[-\frac{(\bar{x}-x)^2}{2q^2}\right] dx \quad (5.8)$$

where $\bar{\alpha}_s$ represents the average attenuation coefficient.

In many cases $(a_{50}-a_{10}) - (a_{84}-a_{50}) \neq 0$, which means the natural size distribution is not symmetric. As an example of an asymmetric distribution, we use the Rayleigh distribution for which this difference is negative. The general expression for the Rayleigh distribution is given by [Bendat 1958, pp. 134-138]

$$n(a) = \frac{\pi a}{2\bar{\alpha}_s^2} \exp\left[-\frac{\pi a^2}{4\bar{\alpha}_s^2}\right] \quad (5.9)$$

where $\bar{\alpha}_s$ is the mean value of sand. For simulating size distributions, we use a *modified* Rayleigh distribution (see Fig. 18):

$$n(a) = \frac{\pi(a-l)}{2\bar{\alpha}_s^2} \exp\left[-\frac{\pi(a-l)^2}{4\bar{\alpha}_s^2}\right] \quad (5.10)$$

where $n(a) = 0$ for $a \leq l$. In Eq. (5.10) $\bar{\alpha}_s$ determines the shape of the distribution. The mean size \bar{a} is given by $(\bar{\alpha}_s + l)$.

We estimate the parameters of the Rayleigh distribution l and $\bar{\alpha}_s$ from the data using

$$l = 1.446 a_{10} - 0.446 a_{84} \quad (5.11a)$$

$$\bar{\alpha}_s = 1.065 (a_{50} - l) \quad (5.11b)$$

which can be obtained from Eq. (5.10) by referring to Fig. 18b.

The Rayleigh distribution in $k_c a$ -space can be written as

$$n(z) = \frac{n(a)}{k_c} = \frac{\pi(z-L)}{2\bar{x}_c^2} \exp\left[-\frac{\pi(z-L)^2}{4\bar{x}_c^2}\right] \quad (5.12)$$

where $z = k_c a$, $\bar{x}_c = k_c \bar{a}$ and $L = k_c l$.

Functions A^2 in Eq. (2.15) and $\bar{\sigma}_c$ in Eq. (4.7) take the forms

$$k_c^2 A^2 = \int_0^\infty \frac{\pi(x-L)x^2 |f_\infty|}{2\bar{x}_c^2} \exp\left[-\frac{\pi(x-L)^2}{4\bar{x}_c^2}\right] dx \quad (5.13)$$

and

$$\frac{\rho'_c \bar{\sigma}_c}{k_c M} = \int_0^\infty \frac{3\text{Im}[f_\infty(0)]}{4x^2} \frac{\pi(x-L)}{2\bar{x}_c^2} \exp\left[-\frac{\pi(x-L)^2}{4\bar{x}_c^2}\right] dx \quad (5.14)$$

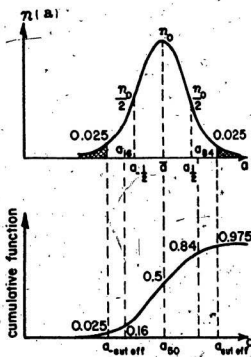
The Gaussian distribution has two infinite tails, and the Rayleigh distribution has one infinite tail. Cutoff sizes had to be chosen prior to numerical integration. These sizes were based on the following formula:

$$\int_{-\infty}^{-a_{\text{cutoff}}} n(a) da + \int_{a_{\text{cutoff}}}^\infty n(a) da < 0.05 \quad (5.15a)$$

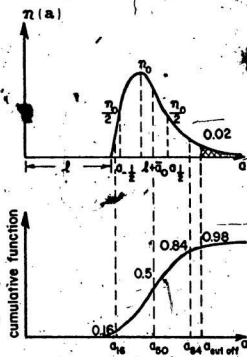
for the Gaussian distribution, and

$$\int_{a_{\text{cutoff}}}^\infty n(a) da < 0.02 \quad (5.15b)$$

for the Rayleigh distribution.



a. Gaussian distribution



b. Rayleigh distribution

Figure 18. The Gaussian and Rayleigh distributions. Here a_{cutoff} and a_{cutoff} is the lower and upper cutoff size, respectively, n_0 is the amplitude of $n(a)$. The remaining symbols are defined in the text.

5.2.5 Estimating sand size distribution parameters

Jansen gave only the nominal mesh openings for the sieves used to obtain each size fraction. In order to specify the size distribution parameters, it is assumed here that the lower and upper sieves correspond to a_{16} and a_{84} respectively. For the Gaussian distribution the above assumption is equivalent to assuming that the sieve boundaries correspond to the half amplitude points of the size spectral density $n(a)$. The values of σ in the two cases differ by a factor of only 1.2. Schaafsma and der Kinderen gave the values of a_{16} , a_{50} and a_{84} . For the data of Clarke et al., a_{16} and a_{84} were estimated from the size distributions given in their paper. The size distribution parameters for each data set are given in Table 5.

Table 5. The size distribution parameters.

Source	k	Size Range (μm)	Gaussian		Rayleigh	
	$10^4 (\text{m}^{-1})$		q	\bar{x}	\bar{x}_s	\bar{x}
Jansen (a)	3.43	45-63	0.31	1.8	0.60	1.87
		105-125	0.35	3.94	0.69	3.99
		175-210	0.61	6.60	1.21	6.68
		250-300	0.86	9.43	1.81	9.51
Schaafsma & der Kinderen (b1)	1.95	38-60	0.22	0.96	0.45	1.00
		55-108	0.52	1.54	0.99	1.60
		65-125	0.59	1.93	1.27	2.01
Schaafsma & der Kinderen(b2) (b2)	1.95	34-70	0.38	0.96	0.67	1.00
		53-120	0.66	1.45	1.08	1.52
		75-160	0.84	1.93	1.29	2.00
Clarke et al. (c1)	1.27	50-90	0.28	0.89	0.51	0.92
		90-150	0.38	1.52	0.76	1.57
		200-288	0.58	3.10	1.14	3.17
(b2)	1.27	37-55	0.12	0.59	0.24	0.60
		70-90	0.14	1.03	0.27	1.05
		153-227	0.48	2.42	0.95	3.43

5.2.6 Comparison with data using size distributions

The numerical values of $\bar{\sigma}_s/\epsilon$ for the Gaussian and Rayleigh distributions were evaluated using the parameters given in Table 5. The theoretical and measured values of $\bar{\sigma}_s/\epsilon$ are given in Table 6a for the Gaussian distribution and in Table 6b for the Rayleigh distribution. These results may be compared with those for uniform size in Table 4. The changes are small, so that the diagrams corresponding to Fig. 16 show little change, and are not presented.

In order to determine which of the theoretical models is most consistent with the data, the root mean square (rms) error was calculated from the differences between the measured and predicted values of $\bar{\sigma}_s/\epsilon$. These are listed in Table 7a. The general tendency is that the rms error is smaller when the size distribution is included. The rms error for the Rayleigh distribution in Table 7a, however, has the same value as that for uniform particle size. This result is in contradiction with what we expected. The rms error of Schaafsma and der Kinderen's experiments alone (Table 7b), however, are smaller for both the Gaussian and the Rayleigh distributions, as expected. The reason that this is not always true when all of the data are included appears to be that Jansen's sand fractions are narrower, so that the changes in rms error due to including either distribution are small for this case (Table 7a). Overall, the rigid movable model with a Gaussian distribution provides the best fit to the data, and when size distributions are included, the rigid immovable and elastic models provide the worst fits. The high-pass model appears to be a useful approximation.

Table 6a. Calculated and measured values of $\bar{\sigma}\bar{\sigma}_s/\epsilon$ for the Gaussian size distribution. Data sources: (a) Jansen, 1977, 1979; (b1) 1-D and (b2) 2-D from Schaafsma and der Kinderen, 1985. "Movable" and "Immovable" represent the rigid movable case and the rigid immovable case, respectively.

Sand			$\bar{\sigma}\bar{\sigma}_s/\epsilon$				
Source	$\bar{\sigma}$ (μm)	$k_s \bar{\sigma}$	Elastic	Movable	Immovable	High-pass	Measured
(a1)	54	1.84	0.262	0.261	0.275	0.285	0.256, 0.178
	115	3.94	0.486	0.465	0.452	0.592	0.566, 0.531
	193	6.60	0.448	0.543	0.540	0.692	0.706, 0.522
	275	9.43	0.733	0.588	0.588	0.724	0.655
(b1)	50	0.96	0.065	0.070	0.105	0.072	0.067
	80	1.54	0.179	0.182	0.213	0.197	0.168
	100	1.93	0.272	0.268	0.276	0.288	0.235
(b2)	50	0.96	0.063	0.068	0.099	0.071	0.075
	75	1.45	0.154	0.156	0.182	0.168	0.176
	100	1.93	0.254	0.246	0.257	0.268	0.242

Table 6b. Calculated and measured values of $\bar{\sigma}\bar{\sigma}_s/\epsilon$ for the Rayleigh size distribution.

Sand			$\bar{\sigma}\bar{\sigma}_s/\epsilon$				
Source	$\bar{\sigma}$ (μm)	$k_s \bar{\sigma}$	Elastic	Movable	Immovable	High-pass	Measured
(a1)	55	1.87	0.260	0.259	0.271	0.283	0.256, 0.178
	116	3.99	0.469	0.463	0.441	0.578	0.566, 0.531
	195	6.67	0.446	0.532	0.529	0.678	0.706, 0.522
	277	9.51	0.719	0.577	0.577	0.711	0.655
(b1)	52	1.00	0.068	0.073	0.109	0.076	0.067
	83	1.60	0.186	0.189	0.220	0.204	0.168
	104	2.00	0.274	0.267	0.279	0.290	0.235
(b2)	54	1.00	0.067	0.072	0.103	0.076	0.075
	79	1.52	0.165	0.168	0.199	0.181	0.176
	104	2.00	0.271	0.264	0.277	0.288	0.242

Table 7a. Root mean square difference between computed and measured values of attenuation coefficient $\bar{\sigma} \bar{\sigma}_c / \epsilon$.

Case	Uniform	Gaussian	Rayleigh
Elastic	0.088	0.086	0.088
Rigid Movable	0.070	0.065	0.070
Rigid Immovable	0.078	0.072	0.078
High-Pass	0.067	0.065	0.061

Table 7b. Root mean square difference between computed and measured values of attenuation coefficient $\bar{\sigma} \bar{\sigma}_c / \epsilon$ (considering Schaafsma and der Kinderen's experiments only)

Case	Uniform	Gaussian	Rayleigh
Elastic	0.030	0.019	0.022
Rigid Movable	0.029	0.016	0.019
Rigid Immovable	0.047	0.032	0.039
High-Pass	0.043	0.027	0.033

5.3 Measured and theoretical scattering coefficients

For suspensions which are sufficiently dilute that $4\alpha_s r_s \ll 1$, the exponential factor in Eq. (2.70) is nearly unity, and

$$\bar{p}_s^2 \approx S^2 H_s^2 \quad (5.16)$$

where S^2 is given in Eq. (2.71), and is determined by the geometry of the system.

From Eq. (2.14) it can be seen that when the frequency is fixed H_s^2 is a function of sand size and concentration. The relationship between H_s^2 and M in Eq. (2.14) is linear, so that H_s^2/M is a function of sand size only. The theoretical results for H_s^2/M as a function of dimensionless radius $k_s a$, for the four theoretical models are shown in Fig. 19 for a bistatic system with $f = 8$ MHz and $\theta = 120^\circ$ and for quartz in water, assuming uniform size. For uniform size Eq. (2.14) becomes

$$H_s^2 = \frac{3M |f_\infty|^2}{4\pi\rho_s a} \quad (5.17)$$

It can be seen that H_s^2/M increases with scatterer radius in the Rayleigh region ($|f_\infty| \sim (k_s a)^2$), and is inversely proportional to the radius in the geometric region ($|f_\infty| \sim 1$), and the maximum amplitude of H_s^2/M can be obtained when the mean particle circumference is approximately equal to the sound wavelength (or when z is in the Mie range), which can be seen from Fig. 19. It is also seen that H_s^2/M for the high-pass model represents a smoother version of

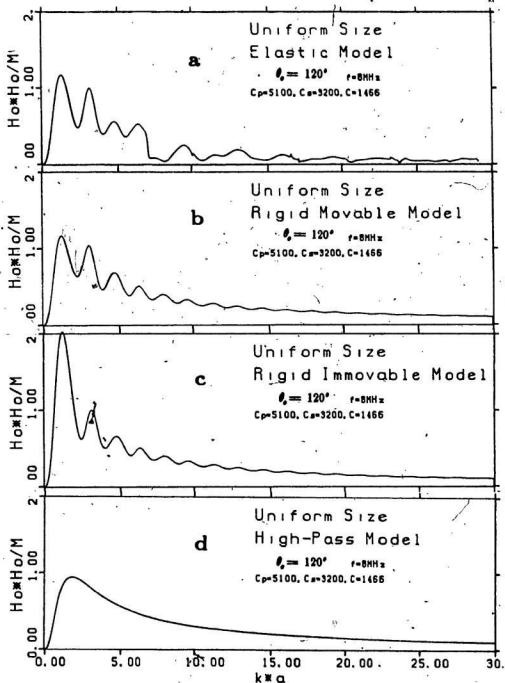


Figure 10 Theoretical estimates of H_0^2/M^2 vs x for uniform size.
 (a) elastic case; (b) rigid movable case; (c) rigid immovable case; (d) high-pass model.

the rigid movable case; in the rigid immovable case H_s^2/M has a very sharp peak in the Mie region while in the elastic case it exhibits additional fluctuating behaviour, which is due to resonances.

The measured values of the mean square scattered signal $\overline{V_s^2}$ at low concentrations were obtained graphically from the results given by Jansen [1977], Schaafsma and der Kinderen [1985] and Clarke et al. [1984] and are listed in Table 8. The values of $\overline{V_s^2}$ in Table 8 for Jansen's experiments are the values at $M = 0.2 \text{ kg/m}^3$, for Schaafsma and der Kinderen's experiments are the relative slopes of $\overline{V_s^2}$ with respect to M at low concentrations as reported by them, and for Clarke et al.'s experiments are the values at $M = 0.01 \text{ kg/m}^3$. The theoretical values of H_s^2 for uniform size were obtained from Eqs. (5.17) and (3.6) and are also listed in Table 8, where we set $M = 1 \text{ kg/m}^3$ for simplicity. It should be noted that we used $|f_\infty(120^\circ)|$ in the calculation of H_s^2 for Jansen's and Schaafsma and der Kinderen's sand fractions, while we used $|f_\infty(180^\circ)|$ for the Clarke et al. sand fractions.

Measurements of absolute scattered intensity (or mean squared scattered pressure) have not been made. Instead, the experiments to date have determined the mean square voltage output from the receiver. Such measurements are proportional to the scattered intensity and the proportionality constant will be different for different data sources. These constants will be removed, however, if we normalize the mean square voltage by its average value for each data set. For comparison, the theoretical estimates of H_s^2 were also normalized by the average values taken over all fractions. The normalized values of H_s^2 and $\overline{V_s^2}$ are shown

Table 8. Calculated values of H_s^2 assuming uniform particle size and measured values of mean square scattered signal V_s^2 . Data sources: (a) Jansen, [1977]; (b1) 1-D and (b2) 2-D from Schaafsma and der Kinderen, [1985]; (c1) major axis and (c2) minor axis from Clarke et al., [1984]. "Movable" and "Immovable" refer to the rigid movable case and rigid immovable case, respectively.

Sand			$H_s^2 (M = 1 \text{ kg/m}^3)$				V_s^2
Source	$\bar{\sigma}$ (μm)	$k_s \bar{\sigma}$	Elastic	Movable	Immovable	High-pass	
(a)	54	1.84	0.852	0.835	1.271	0.944	3650
	115	3.96	0.414	0.464	0.510	0.680	5200
	193	6.60	0.503	0.484	0.481	0.440	4260
	275	9.43	0.246	0.322	0.326	0.319	2690
(b1)	50	0.96	0.905	0.964	1.673	0.658	1.00
	80	1.54	1.112	1.037	1.798	0.922	1.02
	100	1.93	0.757	0.766	1.108	0.942	1.02
(b2)	50	0.96	0.905	0.964	1.673	0.658	1.00
	75	1.45	1.153	1.127	1.914	0.904	1.05
	100	1.93	0.757	0.766	1.108	0.942	0.89
(c1)	70	0.89	0.958	1.004	2.508	0.787	1.13
	120	1.52	0.374	0.311	1.260	1.007	3.63
	244	3.10	1.222	0.647	0.593	0.838	2.60
(c2)	46	0.59	0.513	0.560	1.226	0.427	1.13
	81	1.03	0.982	1.007	2.736	0.904	3.63
	190	2.42	2.508	0.842	1.414	0.968	2.60

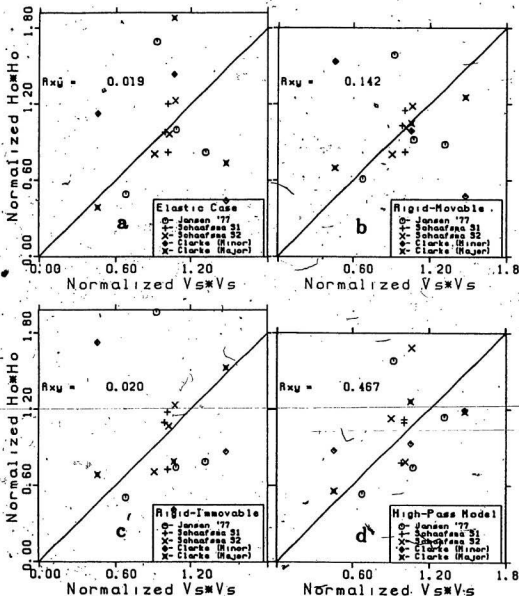


Figure 20. Normalized values of H_o^2 and V_s^2 for uniform particle size.
 (a) elastic case; (b) rigid movable case; (c) rigid immovable case; (d) high-pass model.

in Fig. 20. Comparing this with the attenuation coefficients in Fig. 16, it is seen that there is much greater scatter. This scatter is expected to be reduced when size distributions are included, and to a greater extent than occurred in the case of the attenuation coefficients (compare Fig. 19 with Figs. 21 and 22).

The theoretical estimates of H_s^2/M as a function of dimensionless radius $k_s \bar{r}$ are shown in Fig. 21 for the Gaussian distribution with $q = 0.5$ and in Fig. 22 for the Rayleigh distribution with $\bar{r}_s = 0.8$ for different theoretical models in a bistatic system with $f = 8$ MHz and $\theta = 120^\circ$. These values of q and \bar{r}_s are typical of the experiments (Table 5). Figs. 19, 21 and 22 illustrate the smoothing which occurs at constant frequency, for distributions of constant width. The degree of smoothing is substantial, even for the narrow distributions provided by sieving.

The calculated values of H_s^2 are given in Table 9a for the Gaussian distribution and Table 9b for the Rayleigh distribution, together with the measured values of V_s^2 , and are plotted in normalized form in Figs. 23 and 24, respectively. Comparing these Figures with Fig. 20 indicates that although the degree of scatter is substantially reduced, it is still much worse than for the attenuation coefficients (Fig. 16).

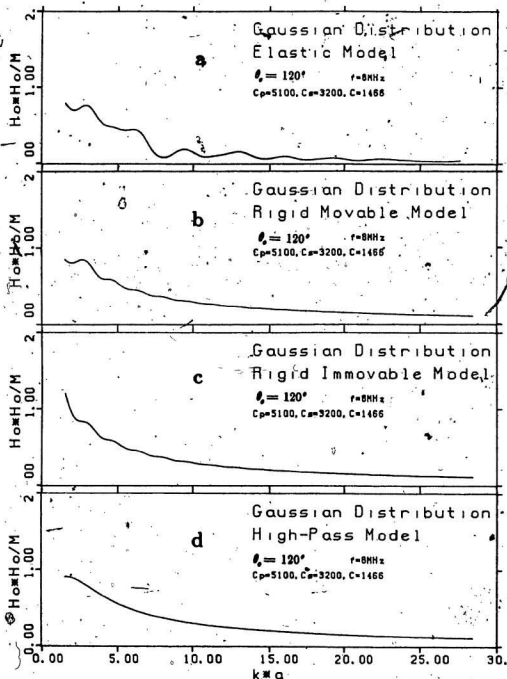


Figure 21. Theoretical estimates of H_0^2/M vs x for the Gaussian distribution: (a) elastic case; (b) rigid movable case; (c) rigid immovable case; (d) high-pass model.

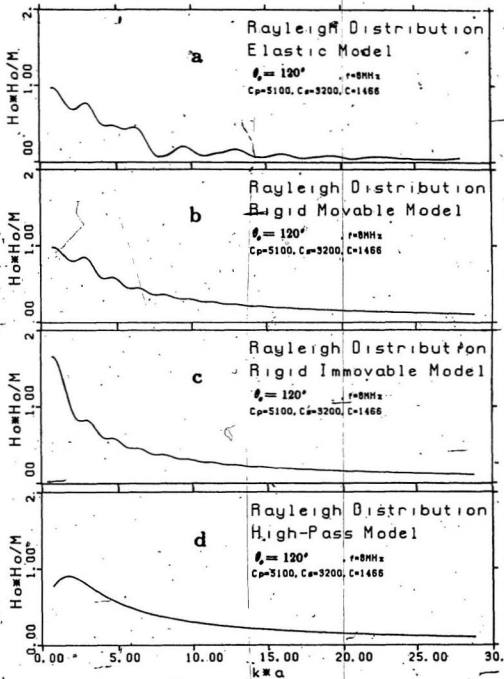


Figure 22. Theoretical estimates of H_0^2/M vs x for the Rayleigh distribution. (a) elastic case; (b) rigid movable case; (c) rigid immovable case; (d) high-pass model.

Table 9a. Calculated values of H_o^2 for the Gaussian size distribution and measured values of mean square scattered signal $\overline{V_s^2}$. Data sources: (a) Jansen, [1977]; (b1) 1-D and (b2) 2-D from Schaafsma and der Kinderen, [1985]; (c1) major axis and (c2) minor axis from Clarke et al., [1984]. "Movable" and "Immovable" represent the rigid, movable case and rigid immovable case, respectively.

Sand			$H_o^2 (M = 1 \text{ kg/m}^3)$				$\overline{V_s^2}$
Source	$\bar{\sigma}$ (μm)	$k_e \bar{\sigma}$	Elastic	Movable	Immovable	High-pass	
(a1)	54	1.84	0.749	0.793	1.116	0.928	3650
	115	3.96	0.495	0.556	0.584	0.673	5200
	193	6.60	0.362	0.420	0.425	0.439	4260
	275	9.43	0.156	0.304	0.307	0.315	2690
(b1)	50	0.96	0.973	1.011	1.751	0.710	1.00
	80	1.54	0.796	0.844	1.219	0.907	1.02
	100	1.93	0.716	0.821	0.954	0.894	1.02
(b1)	50	0.96	1.023	1.036	1.776	0.781	1.00
	75	1.45	0.760	0.834	1.130	0.897	1.05
	100	1.93	0.761	0.845	0.930	0.852	0.89
(c1)	70	0.89	0.830	0.842	2.369	0.882	1.13
	120	1.52	0.952	0.820	1.193	1.043	3.63
	244	3.10	1.599	0.909	0.816	0.801	2.60
(c2)	46	0.59	0.805	0.651	1.478	0.494	1.13
	81	1.03	0.905	0.919	2.583	0.916	3.63
	190	2.42	1.796	0.820	0.987	0.924	2.60

Table 9b. Calculated values of H_o^2 for the Rayleigh size distribution and measured values of mean square scattered signal $\overline{V_s^2}$. Data sources: (a) Jansen, [1977]; (b1) 1-D and (b2)-2-D from Schaafsma and der Kinderen, [1985]; (c1) major axis and (c2) minor axis from Clarke et al., [1984]. "Movable" and "Immovable" represent the rigid movable case and rigid immovable case, respectively.

Sand			$H_o^2 (M = 1 \text{ kg/m}^3)$				$\overline{V_s^2}$
Source	$\bar{\alpha}$ (μm)	$k_s \bar{\alpha}$	Elastic	Movable	Immovable	High-pass	
(a)	55	1.88	0.741	0.797	1.107	0.925	3650
	116	3.98	0.493	0.558	0.585	0.669	5200
	195	6.67	0.343	0.419	0.424	0.436	4260
	277	9.50	0.120	0.243	0.245	0.250	2690
(b1)	52	0.99	1.007	1.029	1.778	0.739	1.00
	83	1.60	0.775	0.845	1.166	0.901	1.02
	104	2.01	0.762	0.848	0.959	0.865	1.02
(b2)	54	1.01	1.013	1.019	1.734	0.794	1.00
	79	1.51	0.777	0.848	1.167	0.895	1.05
	104	2.01	0.763	0.848	0.959	0.863	0.89
(c1)	72	0.92	0.775	0.783	2.253	0.902	1.13
	124	1.57	1.151	0.962	1.235	1.036	3.63
	250	3.17	1.527	0.901	0.796	0.787	2.60
(c2)	47	0.60	0.855	0.687	1.577	0.522	1.13
	83	1.05	0.871	0.887	2.543	0.933	3.63
	269	3.43	1.454	0.804	0.752	0.759	2.60

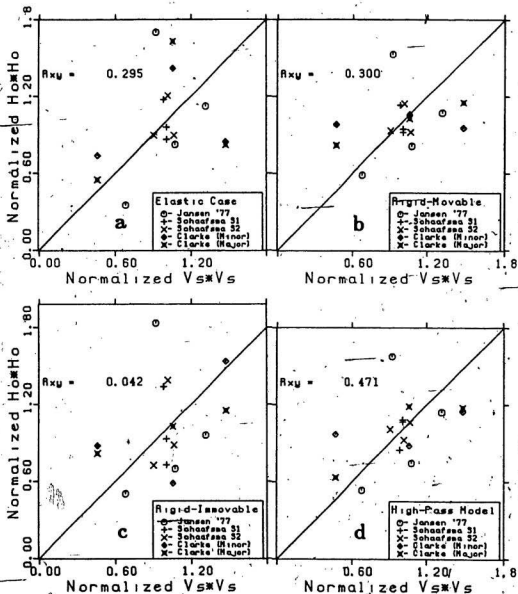


Figure 23. Normalized values of H_0^2 and V_s^2 for the Gaussian distribution.
 (a) elastic case; (b) rigid movable case; (c) rigid immovable case; (d) high-pass model.

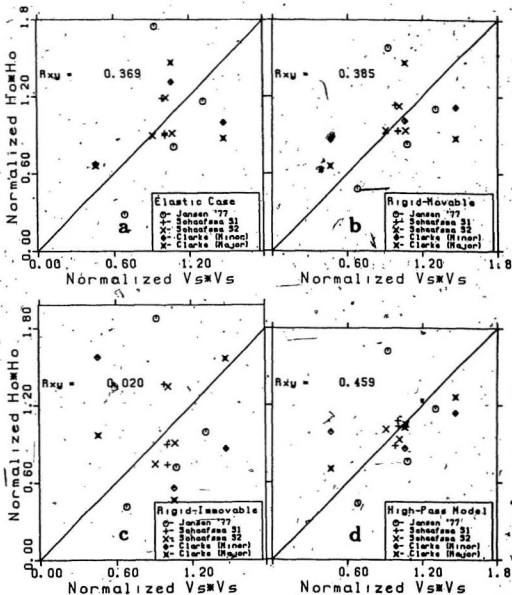


Figure 24. Normalized values of H_o^2 and V_s^2 for the Rayleigh distribution.
 (a) elastic case; (b) rigid movable case; (c) rigid immovable case; (d) high-pass model.

The rms differences between the normalized values of H_o^2 and $\overline{V_o^2}$ are listed in Table 10. It is obvious that agreement between the calculated and measured values is improved by including the size distributions. The rigid movable and high-pass models give the best agreement with experiment. The rigid immovable model provides a poor fit to the data. The rms error for the high-pass model does not change significantly when the size distributions are included, as expected.

Comparing Table 7 and Table 10 it is clear that the effects of size distribution on $\overline{\alpha \alpha_s} / \epsilon$ are smaller than on H_o^2 , although when the Schaafsma and der Kinderen's data are considered alone the effects of size distributions on the attenuation coefficient are seen to be important (Table 7b). It is also clear that the rms difference between theory and experiment is much larger for the scattered intensities than for the attenuation coefficient.

Table 10. Root mean square differences between normalized values of H_o^2 and normalized values of $\overline{V_o^2}$.

Case	Uniform	Gaussian	Rayleigh
Elastic	0.49	0.38	0.35
Rigid Movable	0.43	0.29	0.28
Rigid Immovable	0.51	0.50	0.51
High-Pass	0.31	0.27	0.28

5.4 Discussion

In this chapter we compared the calculated values of both $\bar{\alpha}\bar{\alpha}_s/c$ and H_s^2 with data. It is found that the theoretical results fit the data reasonably well. The more specific conclusions to be drawn from this comparison are the following:

- [1] At this time the experimental attenuation coefficient data provide a better basis for discriminating among the models than scattered intensity, since absolute measurements of attenuation coefficient can easily be obtained from the mean square scattered output signal, and the rms differences between measured and theoretical scattered intensities are much too large.
- [2] There are three theoretical models which contain any physics: these are the elastic, rigid movable and rigid immovable cases. On the basis of the attenuation data, the rigid movable model provides the best fit. This implies that resonance excitation does not occur in natural sand grains, which is not unexpected. For a spherical scatterer, surface trapped waves are excited which propagate around the circumference of the sphere in a time which at resonance represents an integral number of incident wave periods [Flax et al. 1978]. In the presence of irregularities in particle shape and composition, these surface waves will be scattered by the irregularities, and the circuit time will depend on the path around the particle. It appears that for natural sand grains, these irregularities are sufficiently large that well-defined resonant modes do not exist. Finally, comparing the rigid movable and immovable cases, the rms differences between experimental and predicted

attenuation coefficients are larger in the immovable case for the frequency/size range of the measurements, which is primarily in the Mie region. This result implies that the density difference between the sand grains and water is important near $k_z a = 1$.

- [3] The high-pass models for both form factor and attenuation coefficient appear to be useful approximations for real non-uniform sand grains.

The large rms difference between theoretical and experimental scattered intensities represents a problem. We suggest that there are a number of contributing factors. One of these is the error introduced by the normalization procedure, which would not contribute if absolute measurements had been made. A second is that it is difficult to estimate the relative amplitudes of the scattered signals at different radii at constant concentration from the data of Clarke et al. [1984]. Examination of their Fig. 3 shows that these estimates cannot be made unambiguously, either because of scatter in the data or because of non-linear changes with concentration, (even though $M < 0.1 \text{ kg/m}^3$ so that attenuation should not be important). Thirdly, it is possible that in Jansen's experiments the particles adopted a preferred orientation because they were allowed to free fall through the detected volume. In addition, the deflection of acoustic waves by the rectangular tube in Jansen's experiments may have led to additional errors in the measured values of intensity. However, the agreement between theoretical and measured attenuation coefficients using Jansen's data is reasonably good (Fig. 14), and it is difficult to explain how tube effects could cause larger errors in the normalized scattered intensities.

There is another possibility, and that is that although a spherical shape is a

suitable model for the attenuation coefficient even though the particles are irregular, as the comparisons with the data indicate, it may not be for the intensity scattered in a given direction. Clarke et al. [1984] have suggested, on the basis of the bistatic theorem, that for randomly oriented irregular particles, it is more appropriate to estimate the backscattered intensity for a single particle from the total scattered power for a single particle. In effect this implies that the random orientations of the sand grains result, on average, in isotropic scattering. Furthermore, since the total power scattered by a single particle is proportional to α_s , this argument suggests that the effects of random orientation of irregularly shaped grains be accounted for by assuming that $|f_\infty|^2$ at constant concentration is proportional to α_s at constant concentration. Eq. (4.7b). In fact, the geometric similarity between the curves for $a\alpha_s/k_c M$ in Fig. 9 and those for H_s^2/M in Fig. 19 (applying additional visual smoothing in the latter case) indicates that this might be reasonable. This comparison has been made for the case of uniform size, and the results are plotted in Fig. 25. The rms errors are presented in Table 11. Comparing these results with Fig. 20 and Table 10, it is clear that there is considerable improvement in both the rms errors and the correlation coefficients, suggesting that this approach may be quite useful. The degree of scatter is still too great, however, and the data too few, to discriminate among the models.

Table 11. Root mean square differences between normalized values of $\rho_s^2 \alpha_s / K_c M$ and normalized values of V_s^2 .

Case	rms Difference
Elastic	0.35
Rigid Movable	0.32
Rigid Immovable	0.23
High-pass	0.35

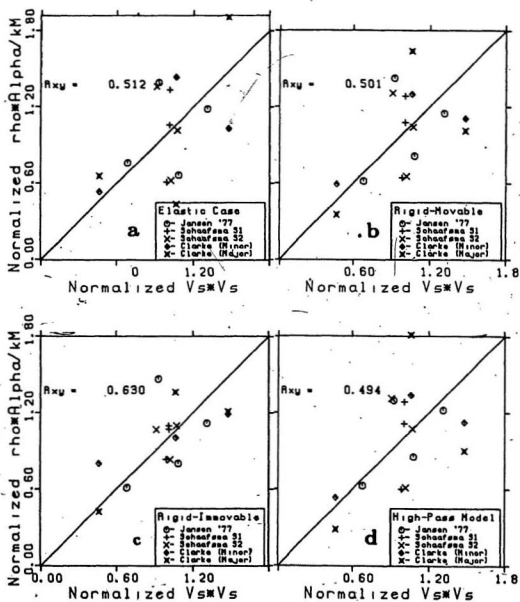


Figure 25. Normalized values of $\rho_s \alpha_s / k_s M$ and $\overline{V_s^2}$
 (a) elastic case; (b) rigid movable case; (c) rigid immovable case; (d) high-pass model.

CHAPTER 6 CONCLUSIONS

The geometric considerations associated with scattering and attenuation in bistatic systems have been analyzed for the narrow beam case. In order to obtain analytic expressions for the detected volume and scattered intensity, we introduced the parabolic approximation, which was compared with exact numerical results for the parameter range of interest. The comparison shows that the errors due to this approximation are within 10% in this parameter range.

We compared the theoretical estimates of scattered intensity and attenuation coefficient in three models with the data presently available. The theoretical estimates were made by approximating the sand grain as a homogeneous, spherical scatterer, and by using the partial wave phase-shift formalism to obtain the scattered pressure field. The three models are: elastic, rigid movable and rigid immovable. We have shown that the rigid movable model with a Gaussian size distribution provides the best fit to the data. The fact that the elastic model does not fit the data as well indicates that resonance excitation does not occur, supporting a similar conclusion made by Clarke et al. [1984]; probably because natural sand grains are irregularly shaped and inhomogeneous in composition. The rigid immovable model fits the data the least well, indicating that the inertia of the particles is important, and that grain density is an important parameter.

It has also been found that while the calculated values of the attenuation coefficient and the data are in reasonable agreement, the normalized theoretical and experimental values of scattered intensity exhibit large rms differences. Several factors which may contribute to these differences have been discussed, but none are conclusive. More extensive data are required.

Approximate expressions for the form factor and attenuation coefficient have been constructed, based on the so-called high-pass model introduced by Johnson [1977]. In Chapter 5 it was seen that the high-pass model provides a fit to the data which is as good as the rigid movable case. Its value is that it provides a simple analytic expression for evaluation of the size and concentration dependence of the scattered signal. Therefore we can use the following formula to express roughly sound scattering in aqueous suspensions of sand:

$$|f_{\infty}| = \frac{K_f z}{1 + K_f z}$$

for the form factor, and


$$\frac{a \alpha_s}{\epsilon} = \frac{K_o z^4}{1 + (4/3)K_o z^4 + z^2}$$

for the attenuation coefficient, where K_f and K_o are constants which depend on the physical properties of the particles and of water, and, in the case of K_f , the scattering angle.

Multiple scattering has been discussed briefly in this thesis. Approximate estimates for the first order correction for multiple scattering were made. It was shown that the non-linear dependence of the attenuation coefficient on concentra-

tion at large M , is due to multiple scattering and that the approximate estimate for the case in which forward scattering dominates ($x \gg 1$) is in reasonable agreement with the data. The predicted effects are too large, however, for $x \sim 1$, due to ignoring the phase shift of the scattered waves and the directivity of the narrow beam transducers is the near-field.

This is the first instance in which comparisons have been made between theoretical and experimental attenuation coefficients in suspensions of sand in the medium and short wavelength regions. Because the data yield an absolute measure of the attenuation coefficient, the attenuation coefficient represents an important test of the theory. The good agreement between theory and experiment confirms the validity of the spherical model at least with regard to the angular integral of scattered intensity. The principal remaining problem is to explain the high degree of scatter in the comparison between the theoretical and measured scattered intensities. This requires further experimental work, in which the scattered intensity should be measured over a wide frequency range at narrow intervals.



REFERENCES

- Abramowitz, M., & I. A. Stegun, *Handbook of Mathematical Functions*, National Bureau of Standards, Applied Mathematics Series, Dover, **55**, 437-478, 1968.
- Allegra, J. R., & S. A. Hawley, Attenuation of Sound in Suspensions and Emulsions: Theory and Experiments, *J. Acoust. Soc. Amer.*, **51(5)**, 1545-1563, 1972.
- Bendat, Julius S., *Principles and Applications of Random Noise Theory*, John Wiley & Sons, 78-184, 1958.
- Beyer, W. H., *Standard Mathematical Tables*, CRC Press, inc., 26th Edition, 510, 1981.
- Booker, H. G., & J. T. de Bettencourt, Theory of Radio Transmission by Tropospheric Scattering Using Very Narrow Beams, *Proc. IRE*, **43**, 281-290, 1955.
- Clarke, S. P., *Handbook of Physical Constants*, Geol. Soc. Am. Mem., **97**, revised ed., 197-201, 1966.
- Clarke, T. L., J. R. Proni & J. F. Craynock, A Simple Model for the Acoustic Cross Section of Sand Grains, *J. Acoust. Soc. Amer.*, **76(5)**, 1580-1582, 1984.
- Clay, C. S., & H. Medwin, *Acoustical Oceanography*, 544 pp., John Wiley, New York, 1977.
- Dietz, R. S., Deep Scattering layer in the Pacific and Antarctic Oceans, *J. Mar. Res.*, **7**, 430-442, 1948.
- Dragonette, L. R., R. H. Vogt, L. Flax & W. G. Neubauer, Acoustic Reflection From Elastic Spheres. II. Transient Analysis, *J. Acoust. Soc. Am.*, **55(6)**, 1130-1129, 1974.
- Epstein, P. S., & R. R. Carhart, The Absorption of Sound in Suspensions and Emulsions, I. Water Fog in Air, *J. Acoust. Soc. Amer.*, **25(3)**, 553-565, 1953.
- Faran, J. J., Jr., Sound Scattering by Solid Cylinders and Spheres, *J. Acoust. Soc. Amer.*, **23(4)**, 405-418, 1951.
- Flax, L., G. C. Gaunard & H. Uberall, Theory of Resonance Scattering, *Physical Acoustics XV*, edited by W. P. Mason and R. N. Thurston (Academic, New York, 1981), Chap. 3, p. 191-294.

- Hay, A. E., & R. W. Burling, On Sound Scattering and Attenuation in Suspensions, with Marine Applications, *J. Acoust. Soc. Amer.*, **72(3)**, 950-959, 1982.
- Hay, A. E., R. W. Burling & J. W. Murray, Remote Acoustic Detection of a Turbidity Current Surge, *Science*, **217(4562)**, 833-835, 1982.
- Hay, A. E., On the Remote Acoustic Detection of Suspended Sediment at Long Wavelengths, *J. Geophys. Res.*, **88(c12)**, 7525-7542, 1983.
- Hay, A. E., & D. G. Mercer, On the Theory of Sound Scattering and Viscous Absorption in Aqueous Suspensions at Medium and Short Wavelengths, *J. Acoust. Soc. Amer.*, **78(5)**, 1761-1771, 1985.
- Hickling, R., Analysis of Echoes From a Solid Elastic Sphere in Water, *J. Acoust. Soc. Amer.*, **34(10)**, 1582-1592, 1962.
- Hickling, R. & N. M. Wang, Scattering of Sound by a Rigid Movable Sphere, *J. Acoust. Soc. Amer.*, **39(2)**, 276-279, 1965.
- Jansen, R. H. J., The in-situ Measurement of Sediment Transport by Means of Ultrasound Scattering, A paper presented at the autumn meeting 1977 of the Dutch Acoustical Society, Utrecht, November 9, 1977. (The English translation is *Rep. 203*, Delft Hydraulics Laboratory, Delft, The Netherlands, 1978). (see also Jansen, R. H. J., An Ultrasonic Doppler Scatterometer for Measuring Suspended Sand Transport, *Ultrasonic International 79, Conference Proceedings*, Graz, Austria, **UI79**, 368-369, 1979).
- Johnson, R. K., Sound Scattering From a Fluid Sphere Revisited, *J. Acoust. Soc. Amer.*, **61(2)**, 375-377, 1977.
- Lamb, H., *Hydrodynamics*, 6th Ed., Dover, New York, p. 659, 1945.
- Ma, Y., V. K. Varadan & V. V. Varadan, Application of Twersky's multiple scattering formalism to a density suspension of elastic particles in water, *J. Acoust. Soc. Amer.*, **75(2)**, 335-339, 1984.
- Morse, P. M., & H. Feshbach, *Methods of Theoretical Physics*, McGraw-Hill, 1953.
- Morse, P. M., *Vibration and Sound*, 2nd Ed., McGraw-Hill, New York, 1948.
- Neubauer, W. G., R. H. Vogt & L. R. Dragonette, Acoustic Reflection From Elastic Spheres. I. Steady-State, *J. Acoust. Soc. Am.*, **55(6)**, 1123-1129, 1974.
- Orr, M. H., & F. R. Hess, Remote Acoustic Monitoring of Natural Suspensate Distributions, Active Suspensate Resuspension, and Slope/Shelf Water Intrusions, *J. Geophys. Res.*, **83**, 4062-4068, 1978.

Proni, J. R., D. C. Rona, C. A. Lauter Jr. & R. L. Sellers, Acoustic Observations of Suspended Particulates Matter in the Ocean, *Nature*, **254**, 413-415, 1975.

Proni, J. R., F. C. Newman, D. C. Rona, D. E. Drake, G. A. Berberian, C. A. Lauter & R. L. Sellers, On the Acoustics for Studying Suspended Oceanic Sediment and for Determining the Onset of the Shallow Thermocline, *Deep-Sea Research*, **23**, 831-837, 1976a.

Proni, J. R., F. C. Newman & R. L. Sellers, Acoustic Tracking of Ocean-Dumped Sewage Sludge, *Science*, **193**, 1005-1007, 1975b.

Rayleigh Lord (J. W. Strutt), *Theory of Sound*, Vol. 2, 2nd Ed., Dover, New York, pp. 236-284D, 1945.

Read, T. M., & K. E. Gubbins, *Applied Statistical Mechanics*, McGraw-Hill, 458-459, 1973.

Schaafsma, A. S., & W. J. G. J. der Kinderen, Ultrasonic Instruments for the Continuous Measurement of Suspended Sand Transport, *Proc. IAHR-Symposium on Measuring Technique in Hydraulic Research*, Delft, (in press), 11pp, 1985.

Sewell, C. J. T., On the Extinction of Sound in a Viscous Atmosphere by Small Obstacles of Cylindrical and Spherical Form, *Phil. Trans. Roy. Soc. (London)*, **A210**, 239, 1910.

Stakutis, V. J., W. Morse, M. Dill & R. T. Beyer, Attenuation of Ultrasound in Aqueous Suspensions, *J. Acoust. Soc. Amer.*, **27(3)**, 539-546, 1955.

Sugai, Iwao, Exact Equation for Tropospheric Scatter Common Volume, *Proc. IEEE*, **35**, 1795-1796, 1965.

Urick, R. J., The Absorption of Sound in Suspensions of Irregular Particles, *J. Acoust. Soc. Amer.*, **20(3)**, 283-289, 1948.

Varadan, V. K., Y. Ma, & V. V. Varadan, A Multiple Scattering Theory for Elastic Wave propagation in Discrete Random Media, *J. Acoust. Soc. Amer.*, **77(2)**, 375-385, 1985.

Vincent, C. A., R. A. Young & D. J. P. Swift, The Relationship between Bedload and Suspended Sand Transport on the Inner Shelf, Long Island, New York, *J. Geophys. Res.*, **87**, 4163-4170, 1982.

Waterman, P. C., & R. Truell, Multiple Scattering of Waves, *J. Math. Phys.*, **2(4)**, 512-538, 1961.

Young, R. A., J. T. Merrill, T. L. Clarke & J. R. Proni, Acoustic Profiling of Suspended Sediments in the Marine Bottom Boundary Layer, *Geophysical Res. Lett.*, **9**, 175-178, 1982.

APPENDIX A The derivations for τ and G^2

Integrating Eq. (2.51) with respect to Z , we have

$$\tau = 4 \int_{-Y_1}^0 dY \int_0^{\infty} \left[A_0 \sqrt{B_0^2(Y+b_0)^2 - X^2} + A_0 \sqrt{B_0^2(Y-b_0)^2 - X^2} + 2C_0 Y \right] dX \quad (\text{A.1})$$

Integrating Eq. (A.1) with respect to X , we get

$$\begin{aligned} \tau = \frac{2}{m_0^3} \int_{-Y_1}^0 \left\{ \beta_0^2 (Y + m_0 r_0)^2 \arcsin \left[\frac{m_0 w}{\beta_0 (Y + m_0 r_0)} \right] \right. \\ \left. - \beta_0^2 (Y - m_0 r_0)^2 \arcsin \left[\frac{m_0 w}{\beta_0 (Y - m_0 r_0)} \right] \right. \\ \left. + m_0 w \sqrt{(\beta_0 + m_0^2 n_0^2) Y^2 + 2 m_0 r_0 \beta_0^2 Y} \right. \\ \left. + m_0 w \sqrt{(\beta_0 + m_0^2 n_0^2) Y^2 - 2 m_0 r_0 \beta_0^2 Y} \right. \\ \left. + 4 m_0^2 n_0 Y w \right\} dY \quad (\text{A.2}) \end{aligned}$$

where w is given in Eq. (2.52).

The integral was evaluated numerically for $10 \text{ cm} \leq r_0 < 60 \text{ cm}$, $10^\circ \leq \gamma_0 \leq 80^\circ$, and $0.5^\circ \leq \beta_0 \leq 3^\circ$. Over this parameter range, the

detected volume is

$$\tau = (5.1 \sim 5.2) \frac{r_o^3 \beta_o^3}{\sin \theta_o} \quad (\text{A.3})$$

Integrating Eq. (2.56) with respect to Z and X , then

$$\begin{aligned} & \frac{1}{\tau} \iiint g(X, Y, Z) d\tau = \\ &= \frac{1}{6m_o^5 r_o^2 \tau} \left\{ 3(k_c a_o)^2 \beta_o^2 (\beta_o^2 + 4m_o^2 n_o^2) \int (s_2 - s_1) Y^4 dY \right. \\ &+ 8(k_c a_o)^2 m_o^2 n_o (3\beta_o^2 + 4m_o^2 n_o^2) \int w Y^3 dY \\ &+ 12(k_c a_o)^2 m_o r_o \beta_o^4 \int (s_2 + s_1) w Y^3 dY \\ &+ 18m_o n_o^2 r_o \beta_o^2 [2\bar{\alpha} r_o + (k_c a_o)^2 m_o^2 + 2] \int (s_2 + s_1) Y^3 dY \\ &+ (k_c a_o)^2 m_o (\beta_o^2 + 12m_o^2 n_o^2) \int w (w_1 + w_2) Y^2 dY \\ &+ 18(k_c a_o)^2 m_o^2 r_o^2 \beta_o^4 \int (s_2 - s_1) Y^2 dY \\ &+ 12m_o^2 n_o^2 r_o^2 \beta_o^2 [8\bar{\alpha} r_o + (k_c a_o)^2 m_o^2 + 8] \int (s_2 - s_1) Y^2 dY \\ &+ 2m_o^2 r_o [(k_c a_o)^2 \beta_o^2 + 24\bar{\alpha} n_o^2 r_o + 24n_o^2] \int w (w_2 - w_1) Y dY \\ &+ 24m_o^2 n_o r_o^2 \beta_o^2 [8\bar{\alpha} r_o + (k_c a_o)^2 m_o^2 + 8] \int w Y dY \\ &+ 12m_o^3 r_o^3 \beta_o^2 [(k_c a_o)^2 \beta_o^2 + 4n_o^2 (\bar{\alpha} r_o + 1)] \int (s_2 + s_1) Y dY \end{aligned}$$

$$\begin{aligned}
 & + (k_e a_e)^2 m_e^3 \int w(w_1 + w_2) [2w^2 + r_e^2 \beta_e^2] dY \\
 & + 3(k_e a_e)^2 m_e^4 r_e^4 \beta_e^4 \int (s_2 - s_1) dY \}
 \end{aligned} \tag{A.4}$$

where

$$s_1 = \arcsin \left[\frac{m_e w}{\beta_e (Y + m_e r_e)} \right] \tag{A.5}$$

$$s_2 = \arcsin \left[\frac{m_e w}{\beta_e (Y - m_e r_e)} \right] \tag{A.6}$$

$$w_1 = \sqrt{(\beta_e^2 + m_e^2 n_e^2) Y^2 - 2m_e r_e \beta_e Y} \tag{A.7}$$

$$w_2 = \sqrt{(\beta_e^2 + m_e^2 n_e^2) Y^2 - 2m_e r_e \beta_e Y} \tag{A.8}$$

The integral in Eq. (A.4) is very tedious, only numerical values have been obtained for $20^\circ \leq \gamma_e \leq 70^\circ$, $5 \text{ cm} \leq r_e \leq 50 \text{ cm}$ and $0.01^\circ \leq \beta_e \leq 3^\circ$.

The results are given in Table 1.

APPENDIX B. The variation of $|f_{\infty}|$ and α_s with

elastic constants

In this appendix the effects of elastic constants on $|f_{\infty}|$ and α_s are considered.

B.1 The variation of $|f_{\infty}|$ with elastic constants

In order to see the variation of $|f_{\infty}|$ with c_p' and c_s' , four different sediments were chosen. They are sandstone quartzite, mineral quartz, granite and granite gneiss, of which the physical properties are given in Table 2. The theoretical values of the form factor for these sand materials have been computed, and are shown in Fig. 26.

It can be seen that the shapes of $|f_{\infty}|$ in all materials are equivalent in both the Rayleigh and Mie regions. In the geometric region the fluctuations of $|f_{\infty}|$ is larger and resonant positions are more closely spaced for the materials with smaller c_p' and c_s' . Referring to Hay and Mercer [1985], we calculated the non-dimensional eigenfrequencies $x_{2,1}$ and $x_{1,2}$ for the first and the second resonances, which are listed in Table 12. It can be seen that $x_{2,1}$ and $x_{1,2}$ become

smaller as c_p and c_s decrease. For $x < \text{MIN}(x_{2,1}) = 3.65$, no resonance exists for any of these materials, and the shapes of $|f_\infty|$ are similar.

Table 12. The non-dimensional eigenfrequencies of the first and the second resonances

Sediment	$x_{2,1}$	$x_{1,2}$
Granitic gneiss	3.65	4.95
Granite	4.98	5.86
Mineral quartz	5.74	7.11
Sandstone quartzite	6.23	7.24

B.2 The variation of α_s with elastic constants

The theoretical results of α_s for the same four materials are plotted in Fig. 27. It can be seen that the shape of α_s for all materials in the Rayleigh and Mie regions have little difference. In the geometric region they are very different, but all of them tend to the same limiting value for larger x . The different behavior of α_s at the same x for the four materials is due to the shift in the positions of the resonances.

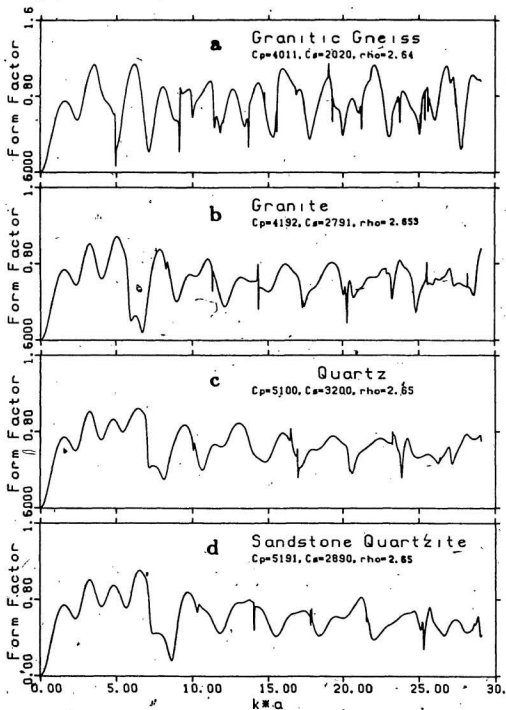


Figure 26. The variation of $|f_\infty|$ in four kinds of sand material.
 (a) granitic gneiss, (b) granite, (c) mineral quartz, (d) sandstone quartzite

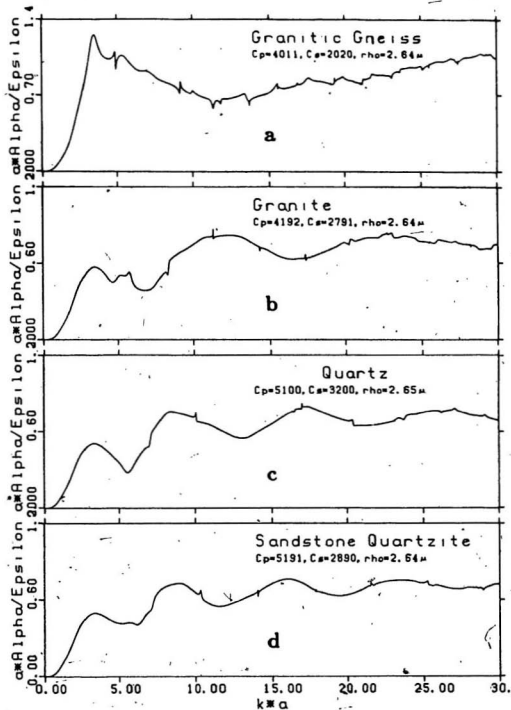


Figure 27. The variation of α_m in four kinds of sand material.
 (a) granitic gneiss, (b) granite, (c) mineral quartz, (d) sandstone quartzite



